materials

MDPI

Review

Review of Systematic Tendencies in (001), (011) and (111) Surfaces Using B3PW as Well as B3LYP Computations of $BaTiO_3$, $CaTiO_3$, $PbTiO_3$, $SrTiO_3$, $BaZrO_3$, $CaZrO_3$, $PbZrO_3$ and $SrZrO_3$ Perovskites

Roberts I. Eglitis [1,*] and Ran Jia [1,2]

[1] Institute of Solid State Physics, University of Latvia, 8 Kengaraga Str., LV1063 Riga, Latvia; jiaran@jlu.edu.cn
[2] Laboratory of Theoretical and Computational Chemistry, Institute of Theoretical Chemistry, Jilin University, Changchun 130023, China
* Correspondence: rieglitis@gmail.com; Tel.: +371-26426703

Abstract: We performed B3PW and B3LYP computations for $BaTiO_3$ (BTO), $CaTiO_3$ (CTO), $PbTiO_3$ (PTO), $SrTiO_3$ (STO), $BaZrO_3$ (BZO), $CaZrO_3$ (CZO), $PbZrO_3$ (PZO) and $SrZrO_3$ (SZO) perovskite neutral (001) along with polar (011) as well as (111) surfaces. For the neutral AO- as well as BO_2-terminated (001) surfaces, in most cases, all upper-layer atoms relax inwards, although the second-layer atoms shift outwards. On the (001) BO_2-terminated surface, the second-layer metal atoms, as a rule, exhibit larger atomic relaxations than the second-layer O atoms. For most ABO_3 perovskites, the (001) surface rumpling *s* is bigger for the AO- than BO_2-terminated surfaces. In contrast, the surface energies, for both (001) terminations, are practically identical. Conversely, different (011) surface terminations exhibit quite different surface energies for the O-terminated, A-terminated and BO-terminated surfaces. Our computed ABO_3 perovskite (111) surface energies are always significantly larger than the neutral (001) as well as polar (011) surface energies. Our computed ABO_3 perovskite bulk B-O chemical bond covalency increases near their neutral (001) and especially polar (011) surfaces.

Keywords: B3PW and B3LYP computations; B3LYP functional; B3PW functional; $SrTiO_3$ (001) surface; $BaTiO_3$ (011) surface; $PbTiO_3$ (111) surface; $SrZrO_3$ (001) surface; $PbZrO_3$ (011) surface; surface energies; polar surfaces

check for updates

Citation: Eglitis, R.I.; Jia, R. Review of Systematic Tendencies in (001), (011) and (111) Surfaces Using B3PW as Well as B3LYP Computations of $BaTiO_3$, $CaTiO_3$, $PbTiO_3$, $SrTiO_3$, $BaZrO_3$, $CaZrO_3$, $PbZrO_3$ and $SrZrO_3$ Perovskites. *Materials* **2023**, *16*, 7623. https://doi.org/10.3390/ma16247623

Academic Editors: Johann Bouclé and Matthias Auf der Maur

Received: 20 October 2023
Revised: 8 December 2023
Accepted: 11 December 2023
Published: 13 December 2023

Copyright: © 2023 by the authors. Licensee MDPI, Basel, Switzerland. This article is an open access article distributed under the terms and conditions of the Creative Commons Attribution (CC BY) license (https://creativecommons.org/licenses/by/4.0/).

1. Introduction

Surface as well as interface phenomena, taking place in the ABO_3 perovskites, including the essence of their (001), (011) and (111) surface and interface electronic properties, are very real problems in present-day physics [1–26]. $BaTiO_3$, $CaTiO_3$, $PbTiO_3$, $SrTiO_3$, $BaZrO_3$, $CaZrO_3$, $PbZrO_3$ and $SrZrO_3$ perovskites are the members of the well-known ABO_3 (A = Ba, Ca, Pb, Sr and B = Ti or Zr) perovskite family [27–29]. They all have a colossal amount of technologically essential applications [30–33]. For example, $BaTiO_3$ is an important ABO_3 perovskite ceramic material [34]. It has outstanding dielectric as well as ferroelectric and piezoelectric properties [34]. $CaTiO_3$ is extensively employed in electronic ceramic materials [35]. Cubic CTO is also used as a keystone element of Synroc [35]. $PbTiO_3$ is one of the worldwide most extensively used piezoelectric and ferroelectric materials for technologically important industrial applications [36–38]. $SrTiO_3$ is a perovskite material with a wide-ranging spectrum of functional properties as well as physical phenomena [39]. STO is an adaptable substrate for complex oxide electronics engineering [40]. STO possesses excellent superconducting properties [41] as well as impurity- and vacancy-based magnetism [42]. $BaZrO_3$ perovskite has several industrially important applications in many quite different technology areas [43]. BZO is extensively used, for example, in solid-oxide fuel cells [44] as well as in wireless systems for communications [45]. $CaZrO_3$ is used as an

ionic conductor to manufacture solid electrodes for applications in various fuel cells [46]. Moreover, CZO is used also as a key element for different sensor types [47,48]. $PbZrO_3$ is a very fascinating perovskite, since it is the end point of the $Pb(Zr,Ti)O_3$ alloy system, which is very interesting for numerous important applications in industry [49]. Finally, $SrZrO_3$ has a lot of technological applications [50–53]. For example, in the violet–blue light emission, laser host materials as well as capacitors and oxygen sensors [50–53]. For that reason, it is clear, that during the last twenty-five years, BTO, CTO, PTO, STO, BZO, CZO, PZO and SZO perovskite (001) surfaces have been comprehensively explored theoretically as well as experimentally around the globe [1–3,6,7,11,13,14,16,18,21,23,24,54–81]. It is worth noting that it is relatively easy to compute the neutral ABO_3 perovskite (001) surfaces, since they consist of alternating neutral AO and BO_2 slabs [82–85]. In contrast, it is very difficult to compute the polar ABO_3 perovskite (011) and (111) surfaces, since they consist of charged planes of ABO and O_2 as well as AO_3 and B, respectively. This is main reason why the ABO_3 perovskite charged and polar (011) [86–95] and (111) [96–107] surfaces are considerably less studied than their neutral and relatively simple (001) surfaces [1–3,6,7,11,13,14,16,18,21,23,24,54–85].

For example, the first B3PW calculations, dealing with polar and charged $BaTiO_3$ and $PbTiO_3$ (011) surface structures were performed by Eglitis and Vanderbilt in 2007 [1]. Two years later, Zhang et al. [86,87], at ab initio level, computed the electronic and structural characteristics of five different terminations of cubic PTO (110) polar surface [86,87]. The first ab initio computations for the polar $SrTiO_3$ (011) surface were carried out by Bottin et al. [88]. They computed the atomic as well as electronic structure of a few (1 × 1) $SrTiO_3$ (011) surface terminations [88]. The year after that, Heifets et al. [89] carried out first-principles Hartree–Fock computations for four terminations (Sr, TiO as well as two different O terminations) of the polar STO (011) surface [89]. As the next, Eglitis and Vanderbilt [2] performed hybrid DFT computations for three different terminations (TiO, Sr and O) of the polar and charged STO (011) surface [2]. Two years later, Enterkin et al. [90] described the results for the 3 × 1 extended STO (011) surface structure derived experimentally via transmission electron diffraction [90]. Experimental results, dealing with polar STO (011) surfaces, were also confirmed theoretically using modern ab initio DFT computations as well as scanning tunneling microscopy images [90]. Finally, five years ago, Fleischer et al. [91] experimentally investigated the STO (011) surface using reflectance anisotropy spectroscopy (RAS). World-first ab initio calculations for polar CTO (011) surfaces were performed by Zhang et al. [92]. They constructed four different CTO polar (011) surface terminations and computed the cleavage as well as (011) surface energies [92]. Zhang et al. [92] also computed the CTO (011) surface grand potential as well as the (011) surface electronic and atomic structure [92]. One year later, Eglitis and Vanderbilt, using a B3PW hybrid exchange–correlation functional, investigated three different terminations (TiO, Ca and O) of polar CTO (011) surfaces [3]. They [3] computed the polar CTO (011) surface atomic relaxations, energetics as well as chemical bonding properties for three different (011) surface terminations [3].

Two world-first ab initio simulations for the polar $BaZrO_3$ (011) surfaces were performed independently by Heifets et al. [93] and by Eglitis [82] in 2007. Heifets et al. [93] studied the charge redistribution, atomic and electronic structure of several different terminations of BZO (011) surfaces [93]. According to the B3PW computations performed by Eglitis [82], three different terminations of the BZO (011) surface exhibit quite different surface energies. They always (for all three terminations) are considerably larger [82] than for the neutral BZO (001) surfaces. Eglitis and Rohlfing [94] computed the SZO and PZO neutral (001) and polar (011) surface rumplings, relaxations, energetics, charge redistributions as well as the Γ-Γ band gaps [94]. Four years later, Chen et al. [95] investigated the electronic properties and stabilities of SZO (110) (1 × 1) five different polar terminations [95]. Finally, the only existing B3LYP calculations, dealing with polar CZO (110) surfaces, were recently performed by Eglitis and co-workers [10].

A quarter of century ago, Hagendorf et al. [96], experimentally investigated the polar BTO (111) surface using scanning tunneling microscopy (STM), X-ray photoelectron spectroscopy (XPS) and low-energy electron diffraction (LEED) methods [96]. Recently, Chun et al. [97], explored the BTO surface (111) termination, using the theoretical ab initio DFT calculations and experimental XPS analysis [97]. First-in-the-world ab initio linearized augmented-plane-wave method (LAPW) calculations for periodic (111) BTO slabs were performed by Cohen [98]. Cohen found [98] that the polar (111) BTO slab is considerably less stable than the BTO neutral (001) slab. In 2015, Eglitis [5,60,99] performed very comprehensive B3LYP calculations for BTO, PTO, CTO, STO, PZO and SZO (111) surfaces. Eglitis found [5] that the polar BTO, PTO, CTO, STO, PZO and SZO (111) surfaces are considerably less stable than the respective neutral (001) and even polar (011) surfaces [5,60,99]. Twenty-five years ago, Haruyama et al. [100] experimentally studied the polar STO (111) surface by means of photoemission spectroscopy [100]. In 1999, Pojani et al. [101], by means of simple semi-empirical HF method, computed the polar STO (111) and (110) surfaces [101]. Recently, Torrelles et al. [102] experimentally detected the surface structure of Ti-terminated STO (111) single crystals [102]. Finally, Marks et al. [103] described the reconstructions of the polar STO (111) surface by means of experimental-transmission electron diffraction, scanning tunneling microscopy as well as theoretical first-principles DFT calculations [103]. Pang et al. [104] performed very comprehensive first-principles computations for four different (1 × 1) polar terminations of PTO (111) surfaces. The electronic and structural properties as well as stabilities of four different polar (1 × 1) PTO (111) terminations were calculated at ab initio level [104]. Liu et al. [105] constructed the stoichiometric as well as nonstoichiometric terminations for polar CTO (111) surfaces [105]. They computed the polar CTO (111) surface electronic structure, grand potential as well as the relevant surface and cleavage energies [105]. Kim et al. [106] explored twenty-two low-indexed BZO (001), (011) as well as (111) surface terminations in order to investigate the Gibbs free energy for their surfaces [106]. Finally, Eglitis [107] performed B3LYP computations for BaO_3- and Zr-terminated polar BZO (111) surface relaxations and energetics.

The objective of our review paper was to carry out necessary additional ab initio computations in order to finalize our more-than-20-year-long research work, devoted to ABO_3 perovskite surfaces. Namely, we report in this place our B3PW and B3LYP computation results for BTO, CTO, PTO, STO, BZO, CZO, PZO, SZO neutral (001) as well as polar (011) and (111) surfaces. We meticulously analyzed B3PW and B3LYP computation results and detected systematic tendencies, typical for all eight of our ab initio computed ABO_3 perovskite surfaces. Finally, we systematized these common systematic trends in a system, effortlessly approachable worldwide for a comprehensive audience of scientists.

2. Computational Details and Surface Models

We performed very comprehensive hybrid density functional theory (DFT) calculations for eight different ABO_3 perovskite (001), (011) and (111) surfaces by means of the CRYSTAL [108] computer program. The CRYSTAL computer program [108] utilizes Gaussian-type well-localized basis sets (BSs). The BSs for BTO, PTO and STO perovskites were evolved by Piskunov et al. [109]. Almost all computations in this review were executed by means of the B3PW [110,111] or B3LYP [112] hybrid exchange–correlation functionals. It is worth noting that the hybrid exchange–correlation functionals, like B3PW or B3LYP, enable us to reach an outstanding agreement with the experiment [10,75] for the Γ-Γ band gaps of different ABO_3 perovskites. We executed the reciprocal-space integration for the ABO_3 perovskite bulk and their surfaces by examining the Brillouin zone, utilizing the 8 × 8 × 8 and 8 × 8 × 1 times, respectively, enlarged Pack Monkhorst grid [113]. The trump card of the CRYSTAL computer program [108] is its ability to compute isolated, two-dimensional slabs, without any unnatural periodicity in the direction z, perpendicular to the slab surface. We performed B3PW and B3LYP computations for all eight ABO_3-type perovskites and their surfaces in high symmetry, cubic structure (space group $Pm\bar{3}m$) [114–116].

With the goal of simulating the neutral BO_2-terminated (001) surfaces of ABO_3-type perovskites [114], we selected symmetrical slabs. These slabs, in our computations, consisted of nine neutral and alternating BO_2 as well as AO layers (Figures 1 and 2). The first slab was terminated by the BO_2 planes and was composed of a supercell which accommodated 23 atoms (Figure 1). The second slab was terminated by the AO planes and was composed of a supercell which accommodated 22 atoms (Figure 2). Both these (001) surface slabs are nonstoichiometric. They have unit cell formulas equal to $A_4B_5O_{14}$ and $A_5B_4O_{13}$, respectively (Figures 1 and 2).

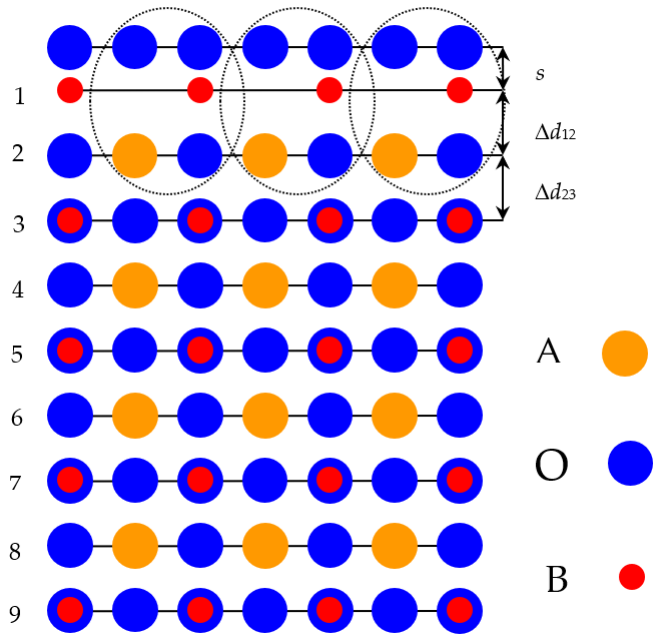

Figure 1. Profile for the BO_2-terminated (001) surface of ABO_3-type perovskite accommodating nine layers and containing the definition of the surface rumpling s as well as the near-surface interplane distances Δd_{12} and Δd_{23}.

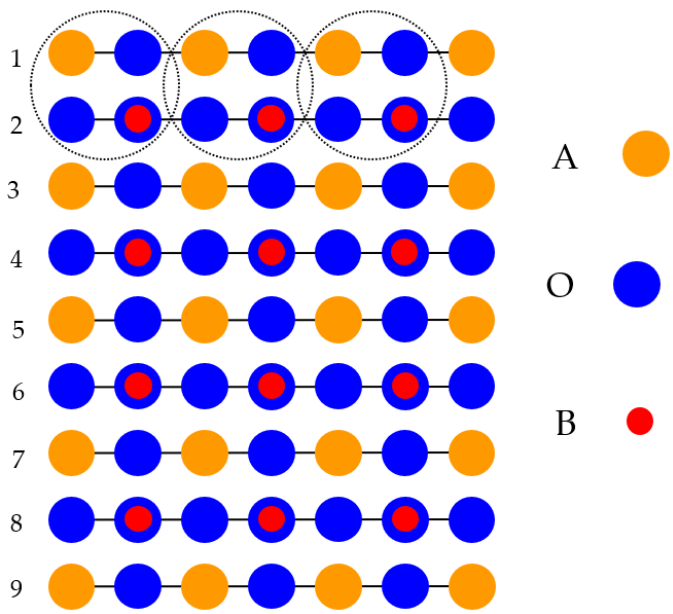

Figure 2. Profile for the AO-terminated (001) surface of ABO_3-type perovskite accommodating nine layers.

Just opposite to the (001) cleavage (Figures 1 and 2) of ABO_3, which produce nonpolar AO and BO_2 terminations, direct cleavage of ABO_3-type perovskites, in order to generate (011) surfaces, leads to the production of polar O_2 as well as ABO surfaces (Figure 3). The ABO_3 crystal (Figure 3), alongside the [011] crystalic direction, is composed of cyclic planes of O_2 and ABO units (Figure 3). These two alternating O_2 and ABO planes (Figure 3) have ionic charges of $-4e$ and $+4e$, assuming following constituents as O^{2-}, B^{4+} and A^{2+}. Therefore, modeling of the ABO_3 (011) surfaces (Figure 3) precisely, as they are obtained from the pristine crystal cleavage, leads to the following two problematic situations: An infinite macroscopic dipole moment, which is perpendicular to the ABO_3 perovskite (011) surface (Figure 4), when the slab is terminated by different O_2 as well as ABO planes (Figure 4) (stoichiometric slab). Infinite charge, in case when the slab is terminated by the same planes (O_2-O_2) (Figure 5) or ABO-ABO (Figure 6) (nonstoichiometric slab). Such ABO_3 perovskite (011) surface terminations (Figures 5 and 6) make the (011) surface unstable [117,118].

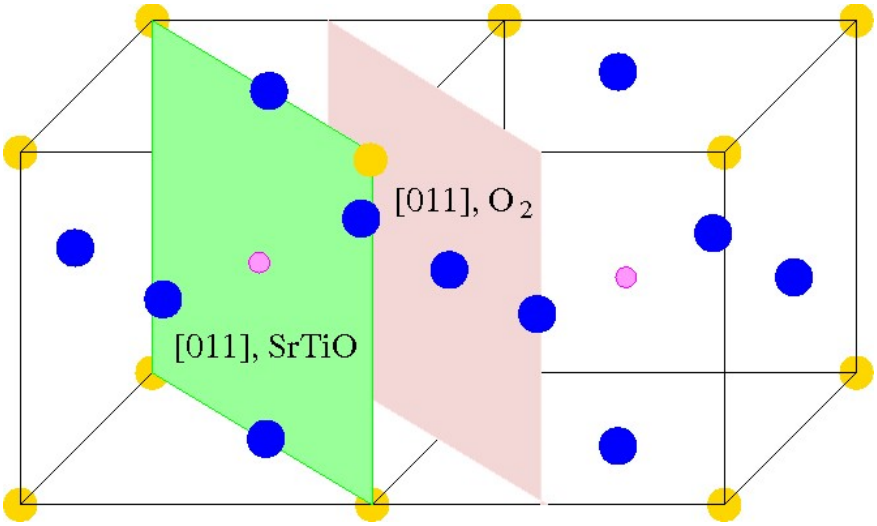

Figure 3. Sketch of the cubic ABO_3 perovskite construction, containing two (011) cleavage planes, consisting of charged O_2 as well as ABO (011) surfaces.

This was the key reason why in our ABO_3-type perovskite (011) surface computations, with the aim of obtaining the neutral (011) slab, we deleted some atoms (Figures 7–9). Namely, we deleted the O atom (Figure 9) from the upper as well lower layers of the nine-layer O-O-terminated symmetric nonstoichiometric (011) slab. Thus, we obtain a neutral O-terminated ABO_3 perovskite (011) slab without any dipole moment perpendicular to the slab surface (Figure 9). Similarly, we deleted both B and O atoms (Figure 8) or an A atom (Figure 7) from the upper and lower layers of the ABO-terminated symmetric nonstoichiometric ABO_3 perovskite (011) slabs. Thus, we obtain neutral A-terminated (Figure 8) or BO-terminated (Figure 7) ABO_3 perovskite (011) slabs without any dipole moment perpendicular to their (011) surfaces. Consequently, in our computations, the BO-terminated symmetric, nonstoichiometric (Figure 7) nine-layer (011) slab consisted of a supercell enclosing 21 atoms. The A- (Figure 8) and O- (Figure 9) terminated nonstoichiometric and symmetric ABO_3 perovskite nine-layer (011) slabs consisted of supercells enclosing 19 and 20 atoms, respectively.

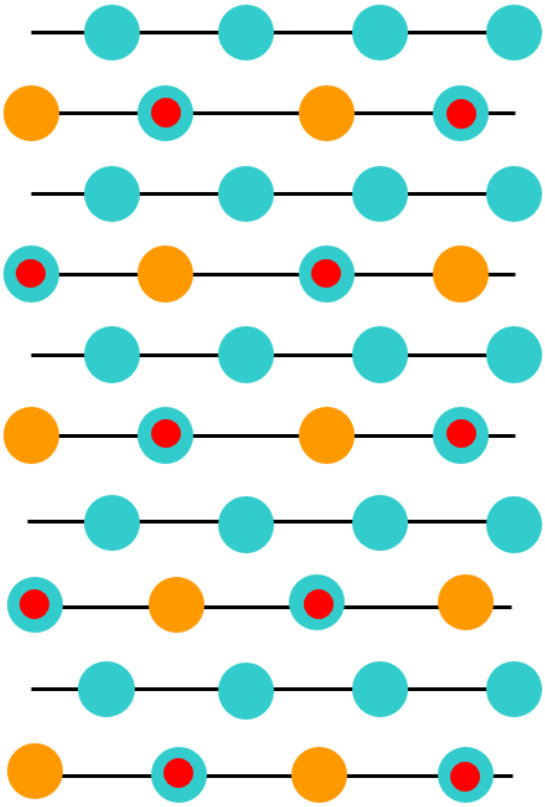

Figure 4. Sketch of the ABO_3 perovskite (011) surface slab models. Slabs are derived by ABO_3 perovskite (011) cleavage yielding mixed O_2 and ABO terminations.

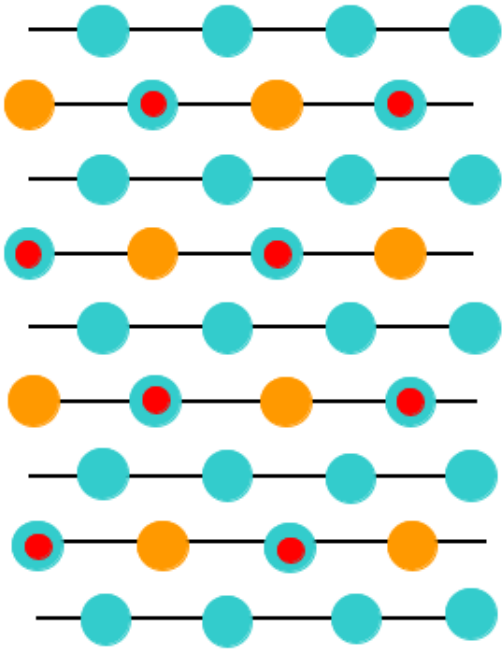

Figure 5. Sketch of the ABO_3 perovskite (011) surface slab models. Slabs are derived by ABO_3 perovskite (011) cleavage yielding an O_2-terminated surface.

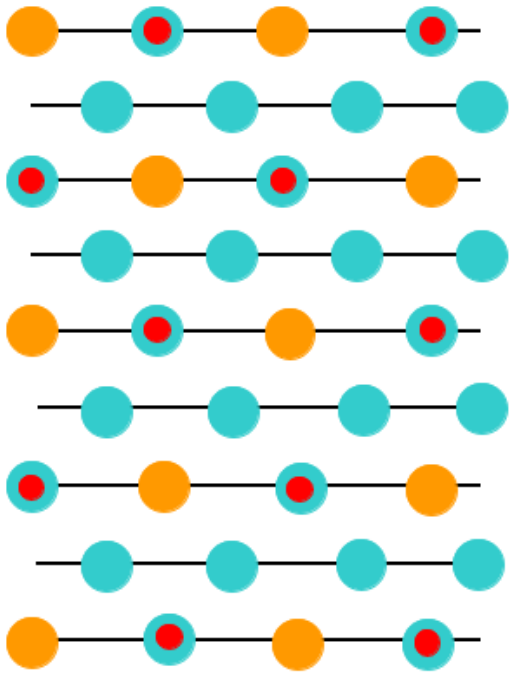

Figure 6. Sketch of the ABO_3 perovskite (011) surface slab models. Slabs are derived by ABO_3 perovskite (011) cleavage yielding an ABO-terminated surface.

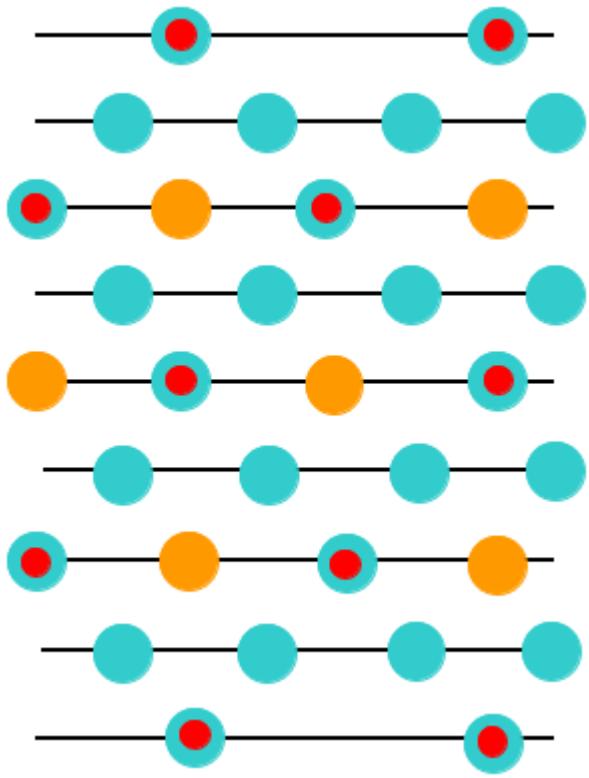

Figure 7. Sketch of the ABO_3 perovskite (011) surface slab models. Slabs are derived by ABO_3 perovskite (011) cleavage yielding a BO-terminated surface.

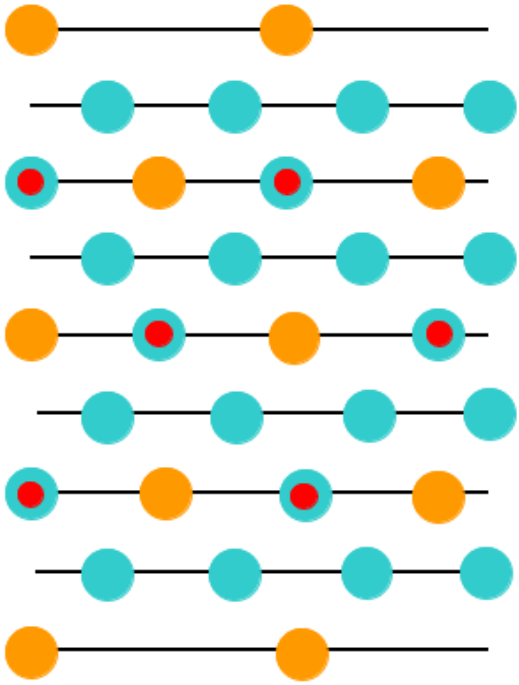

Figure 8. Sketch of the ABO_3 perovskite (011) surface slab models. Slabs are derived by ABO_3 perovskite (011) cleavage yielding an A-terminated surface.

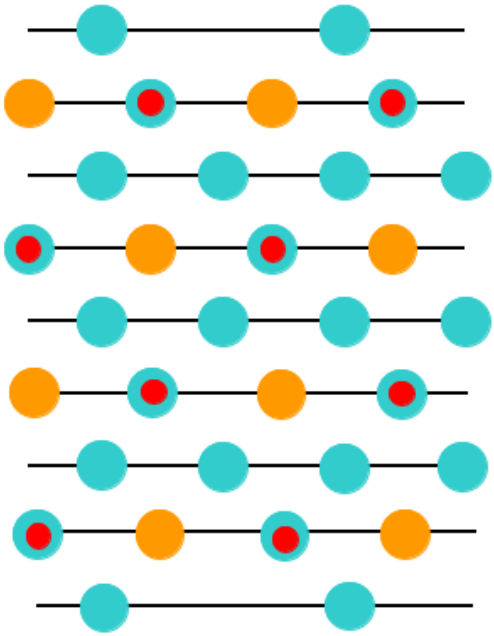

Figure 9. Sketch of the ABO_3 perovskite (011) surface slab models. Slabs are derived by ABO_3 perovskite (011) cleavage yielding an O-terminated surface.

As a further action, the ABO_3 perovskite polar (111) surfaces will be described by us using BZO as an example (Figures 10 and 11) [107]. In order to compute the polar BZO perovskite (111) surfaces, we employed symmetrical, nonstoichiometric (111) slabs containing nine alternating Zr and BaO_3 layers (Figures 10 and 11). One of two BZO (111) slabs (Figure 11a) is terminated by Zr planes from both sides. It consists of a supercell accommodating 21 atoms (Figure 11a). The second (111) slab (Figure 11b) is terminated from both sides by BaO_3 planes. It consists of a supercell accommodating 24 atoms (Figure 11b). Both these Zr- and BaO_3-terminated BZO (111) slabs are symmetrical and

nonstoichiometric (Figure 11). They have the unit-cell formulas $Ba_4Zr_5O_{12}$ and $Ba_5Zr_4O_{15}$, respectively (Figure 11). As we know from studies dealing, for example, with polar STO and CTO (111) surfaces [99,101,119], a strong electron redistribution happens for such (111) terminations (Figure 11) canceling the polarity. Therefore, such calculations are possible for the Zr- or BaO_3-terminated BZO (111) surface [99,101,119]. It is worth noting that we used the basis sets for neutral Ba, Zr and O atoms in all our B3LYP computations dealing with polar $BaZrO_3$ perovskite (111) surfaces [5,99,107].

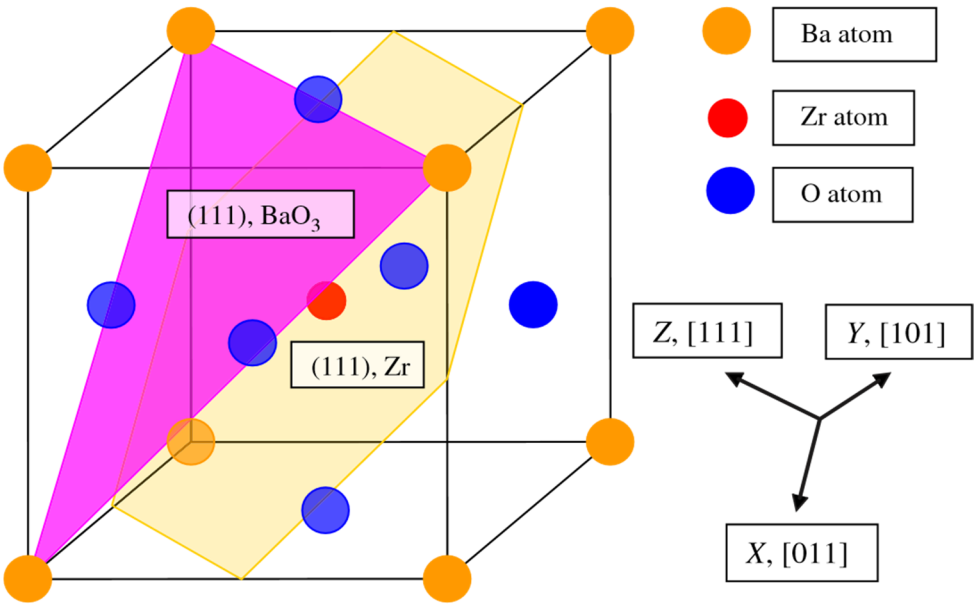

Figure 10. Cubic BZO perovskite structure exhibiting two (111) surface terminations: BaO_3 and Zr.

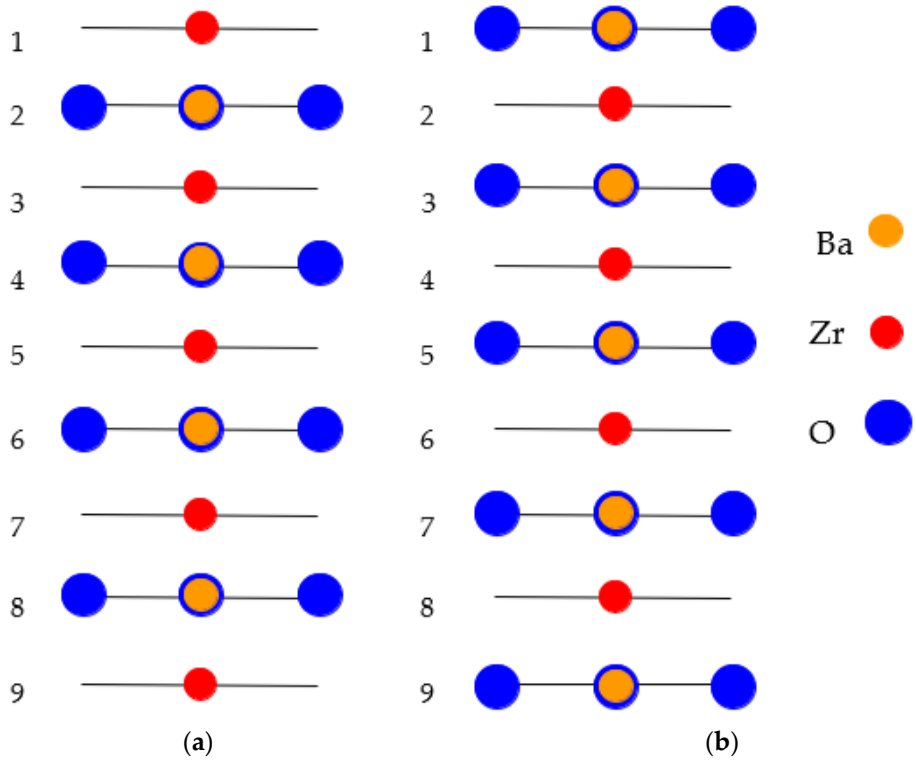

Figure 11. Profile of slab geometries employed to explore BZO (111) surfaces. (**a**) Nonstoichiometric BZO slab containing nine layers with Zr-terminated (111) surfaces. (**b**) Nonstoichiometric BZO slab containing nine layers with BaO_3-terminated (111) surfaces.

With the ultimate goal of computing the ABO_3-type perovskite, for example, the $PbZrO_3$ (001) surface energy, we started our B3LYP computations with the cleavage energy calculations for unrelaxed PbO- as well as ZrO_2-terminated (001) surfaces [1–3,94]. Surfaces with both PbO and ZrO_2 (001) terminations at the same time emerge under the (001) cleavage of the PZO crystal [1–3,94]. We suppose that the PZO perovskite cleavage energy is uniformly shared between the created (001) surfaces (Figures 1 and 2) [1–3]. In our B3LYP computations, the nine-layer PbO-terminated PZO (001) slab with 22 atoms as well as the nine-layer ZrO_2-terminated PZO (001) slab, containing 23 atoms, together contain nine bulk unit cells or 45 atoms atoms, thus:

$$E_{surf}{}^{unr}(\vartheta) = ¼\,[E_{slab}{}^{unr}(PbO) + E_{slab}{}^{unr}(ZrO_2) - 9E_{bulk}], \quad (1)$$

where ϑ means PbO or ZrO_2; $E_{slab}{}^{unr}(\vartheta)$ is the SrO- or ZrO_2-terminated PZO (001) slab energies without relaxation; E_{bulk} is the PZO bulk unit cell, containing five atoms, total energy; and the factor of 1/4 means that we created four surfaces due the PZO crystal (001) cleavage [1–3]. After this, we can compute the relaxation energies for both PbO- and ZrO_2-terminated PZO (001) slabs [1–3,75,82], using the following equation:

$$E_{rel}(\vartheta) = ½\,[E_{slab}{}^{rel}(\vartheta) - E_{slab}{}^{unr}(\vartheta)], \quad (2)$$

where $E_{slab}{}^{rel}(\vartheta)$ is the (001) slab total energy after geometry relaxation [1–3,75,82]. The surface energy is thereby described as a sum of the relevant relaxation as well as cleavage energies:

$$E_{surf}(\vartheta) = E_{surf}{}^{unr}(\vartheta) + E_{rel}(\vartheta). \quad (3)$$

With goal of computing the PZO (011) surface energies for the ZrO- and Pb-terminated (011) surfaces, we think about the cleavage of eight PZO bulk unit cells, in order to obtain the ZrO- and Pb-terminated (011) slabs, which contain 21 and 19 atoms. Namely, we split the cleavage energy uniformly among these two surfaces and derive:

$$E_{surf}{}^{unr}(\vartheta) = ¼[E_{slab}{}^{unr}(Pb) + E_{slab}{}^{unr}(ZrO) - 8E_{bulk}], \quad (4)$$

where ϑ indicates Pb or ZrO; $E_{slab}{}^{unr}(\vartheta)$ is our computed total energy for the unrelaxed Pb- or ZrO-terminated PZO (011) slabs; and E_{bulk} is our computed $PbZrO_3$ perovskite total energy per five-atom bulk unit cell.

In the end, when we cut the PZO perovskite crystal in other way, we obtain two equal O-terminated PZO (011) surface slabs. Each of them contains 20 atoms [1–3,82]. This permits us to make our computations less complex, taking into account that the unit cell of the nine-plane O-terminated PZO (011) slab includes four PZO bulk unit cells [1–3,82]. Thereby, the O-terminated PZO perovskite (011) surface energy is described as follows:

$$E_{surf}(O) = ½\,[E_{slab}{}^{rel}(O) - 4E_{bulk}], \quad (5)$$

where $E_{surf}(O)$ is the O-terminated PZO (011) surface energy, and $E_{slab}{}^{rel}(O)$ is the relaxed O-terminated PZO (011) slab total energy. In the end, the ABO_3 perovskite polar (111) surface energy computation details are described by us in Refs. [5,99,107].

3. Results

3.1. B3PW and B3LYP Calculations of ABO_3 Perovskite Bulk Properties

As a starting point of calculations, we computed the bulk lattice constants for all eight of our considered ABO_3-type perovskites, using two different hybrid exchange–correlation functionals, B3PW and B3LYP. We compared our theoretically computed ABO_3 perovskite bulk lattice constants with available experimental data. Namely, our computed bulk lattice constants, using the B3PW hybrid exchange–correlation functional for BTO (4.008 Å) [1], CTO (3.851 Å) [3], PTO (3.936 Å) [1], STO (3.904 Å) [2], BZO (4.234 Å) [82] and SZO (4.155 Å) [75] perovskites are listed in Table 1. Next, we computed the relevant eight ABO_3

perovskite bulk lattice constants also using the related B3LYP hybrid exchange–correlation functional. Namely, using B3LYP, we obtain the following results for BTO (4.04 Å) [109], CTO (3.851 Å) [99], PTO (3.96 Å) [109], STO (3.94 Å) [109], BZO (4.234 Å) [107], CZO (4.157 Å) [120], PZO (4.220 Å) [94] and SZO (4.195 Å) [94] (Table 1). Experimental ABO_3-type perovskite bulk lattice constants for our eight computed ABO_3 perovskites are collected in Table 1 [121–126] for comparison purposes.

Table 1. Computed ABO_3 perovskite bulk lattice constants [1–3,75,82,94,99,107,109,120] (in Å) by means of the B3PW or B3LYP method. The experimentally detected ABO_3 perovskite bulk lattice constants [121–126] are listed for comparison purposes.

ABO_3-Type Perovskite	B3PW	B3LYP	Experiment
$BaTiO_3$	4.008 [1]	4.04 [109]	4.00 [121]
$CaTiO_3$	3.851 [3]	3.851 [99]	3.8967 [122]
$PbTiO_3$	3.936 [1]	3.96 [109]	3.97 [123]
$SrTiO_3$	3.904 [2]	3.94 [109]	3.89 [121]
$BaZrO_3$	4.234 [82]	4.234 [107]	4.199 [124]
$CaZrO_3$	-	4.157 [120]	-
$PbZrO_3$	-	4.220 [94]	4.1614 [125]
$SrZrO_3$	4.155 [75]	4.195 [94]	4.154 [126]

As we can see from Table 1, both in our computations for ABO_3 perovskite bulk lattice constant used B3PW and B3LYP hybrid exchange–correlation functionals allows us to achieve fair agreement with the experiment [121–126]. For example, the agreement between our B3PW computed $SrZrO_3$ bulk lattice constant 4.155 Å [75] and the experimental value of 4.154 Å [126] is simply outstanding. Also, our B3PW computed BTO bulk lattice constant 4.008 Å [1] is in almost perfect agreement with the experimental data of 4.00 Å [121]. In addition, the agreement between our B3LYP computed $PbTiO_3$ bulk lattice constant (3.96 Å) [109] and the experimental $PbTiO_3$ bulk lattice constant (3.97 Å) [123] is fine.

Our B3PW or B3LYP computed bulk effective atomic charges Q and bond populations P for all eight ABO_3-type perovskites are collected in Table 2. We used the classical Mulliken population analysis [127–130] in order to describe the effective atomic charges Q as well as chemical bond populations P for all eight of our B3PW or B3LYP computed ABO_3-type perovskite materials (Table 2). As we can see from Table 2, our B3PW or B3LYP computed effective atomic charges Q [127–130] are always smaller than those expected from the classical ionic model (+2e for A atoms, +4e for B atoms as well as −2e for O atoms). For example, the A atom effective charges (Table 2) are in the range of only +1.354e for the PTO perovskite to +1.880e for the SZO perovskite (Table 2). The B atom effective charges are in the range (Table 2) from +2.111e for PZO to +2.367e for BTO perovskite. The O atom effective charges [127–130] are between −1.160e for PZO perovskite (Table 2) and −1.407e for the STO perovskite. Finally, the smallest B-O chemical bond population P, according to our B3PW computations, is observed between the Ti-O atom in the CTO perovskite (+0.084e), whereas the largest is between the Zr-O atoms in the BZO perovskite (+0.108e) (Table 2).

Our B3PW computed bulk Γ-Γ band gap for the BTO perovskite is equal to 3.55 eV (Table 3 and Figure 12a). No experimental data exist for the BTO bulk Γ-Γ band gap at the cubic phase. Nevertheless, the related Γ-Γ BTO bulk electronic band structure, measured in the tetragonal towards orthorhombic phase transition temperature [131], identical to 278 K, at contrasting experimental situations, is equivalent to 3.27 or 3.38 eV, respectively. Our B3PW [75] and B3LYP [99] computed CTO bulk Γ-Γ band gaps are almost identical (4.18 eV and 4.20 eV, respectively). Again, there are no experimental data available for the high-temperature cubic CTO phase [75]. It is worth noting that our PWGGA computed CTO bulk Γ-Γ band gap is very small, only 2.34 eV [75], whereas our HF computed CTO bulk Γ-Γ band gap is 5.4 times larger and is equal to 12.63 eV (Table 3). Our B3PW computed PTO bulk Γ-Γ band gap [114] is equal to 4.32 eV (Table 3 and Figure 12b). Our B3PW computed

BZO bulk band structure is plotted in Figure 13. Our B3PW computed STO Γ-Γ bulk band gap 3.96 eV [114] is almost in perfect agreement with the available experimental data for the STO cubic phase at Γ-point 3.75 eV [132] (Table 3 and Figure 14). Our B3PW computed BZO bulk band gap at Γ-point is equal to 4.93 eV [75] and is in fair agreement with the relevant experimental data (5.3 eV) [133]. As we can see from Table 3, PWGGA computed BZO bulk band gap at Γ-point is considerably underestimated (3.24 eV), whereas the HF result (12.96 eV) is considerably overestimated regarding the experimental BZO bulk band gap value of 5.3 eV. Finally, for SZO perovskite, our B3PW and B3LYP computed bulk Γ-Γ band gaps almost coincide (5.30 eV and 5.31 eV, respectively) (Table 3) [75,94]. Our B3LYP computation results, dealing with eight ABO_3-type perovskite bulk Γ-Γ band gaps, are depicted in Figure 14. As we can see from Figure 14, the best possible agreement between the theory and experiment for eight ABO_3-type perovskite bulk Γ-Γ band gaps is possible to achieve by means of the hybrid exchange–correlation functionals, for example B3PW or B3LYP (Table 3 and Figure 14). The HF method hugely overestimated the Γ-Γ bulk band gaps for all eight our computed ABO_3 perovskites, whereas the density functional theory based PWGGA functional underestimated them (Figure 14 and Table 3).

Table 2. BTO, CTO, PTO, STO, BZO, CZO, PZO and SZO perovskite bulk effective atomic charges *Q* (in *e*) and bond populations *P* (in *e*) computed using the hybrid B3PW or B3LYP exchange–correlation functionals [1–3,82,94].

		BTO	**CTO**	**PTO**	**STO**	**BZO**	**CZO**	**PZO**	**SZO**
Ion	**Prop.**	**B3PW**	**B3PW**	**B3PW**	**B3PW**	**B3PW**	**B3LYP**	**B3LYP**	**B3LYP**
A	*Q*	+1.797	+1.782	+1.354	+1.871	+1.815	+1.787	+1.368	+1.880
	P	−0.034	+0.006	+0.016	−0.010	−0.012	+0.014	+0.030	+0.002
O	*Q*	−1.388	−1.371	−1.232	−1.407	−1.316	−1.310	−1.160	−1.351
	P	+0.098	+0.084	+0.098	+0.088	+0.108	+0.086	+0.106	+0.092
B	*Q*	+2.367	+2.330	+2.341	+2.351	+2.134	+2.144	+2.111	+2.174

Table 3. B3LYP, B3PW, HF and PWGGA computed Γ-Γ band gaps (in eV) for eight ABO_3 perovskites. Experimental bulk Γ-Γ band gaps at ABO_3 perovskite cubic phase are listed for comparison purposes.

Perovskite	**Theoretical Method**	**Bulk Band Gap**	**Experiment**
$BaTiO_3$	B3PW	3.55 [114]	No data for cubic phase
$CaTiO_3$	B3PW B3LYP PWGGA HF	4.18 [75] 4.20 [99] 2.34 [75] 12.63 [75]	No data for cubic phase
$PbTiO_3$	B3PW	4.32 [114]	No data for cubic phase
$SrTiO_3$	B3PW	3.96 [114]	3.75 [132]
$BaZrO_3$	B3PW B3LYP PWGGA HF	4.93 [75] 4.79 [107] 3.24 [75] 12.96 [75]	5.3 [133]
$CaZrO_3$	B3LYP	5.40 [120]	No data for cubic phase
$PbZrO_3$	B3LYP	5.63 [94]	No data for cubic phase
$SrZrO_3$	B3PW B3LYP PWGGA HF	5.30 [75] 5.31 [94] 3.53 [75] 13.54 [75]	No data for cubic phase

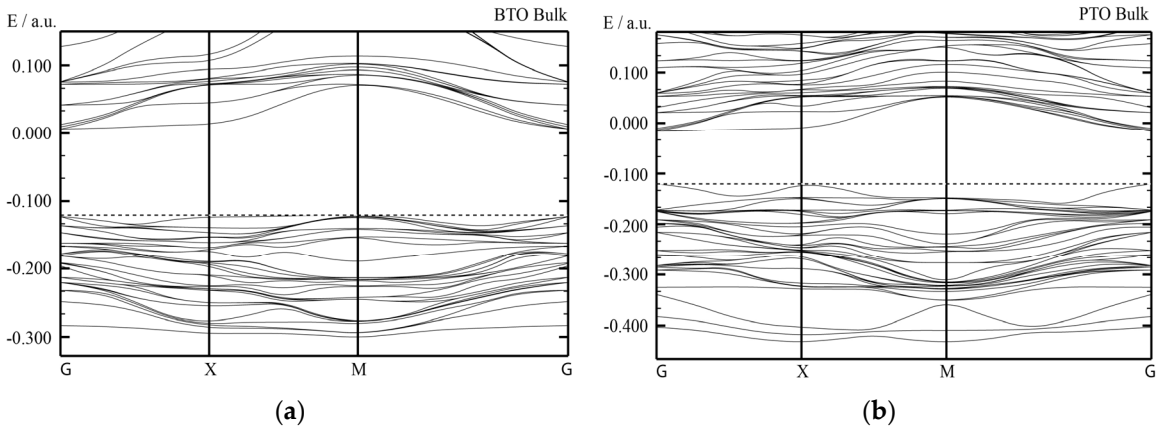

Figure 12. Our hybrid B3PW computed [114] bulk electronic band structure for BTO (**a**) as well as PTO (**b**) perovskites. The dotted lines correspond to the bulk valence band maximum.

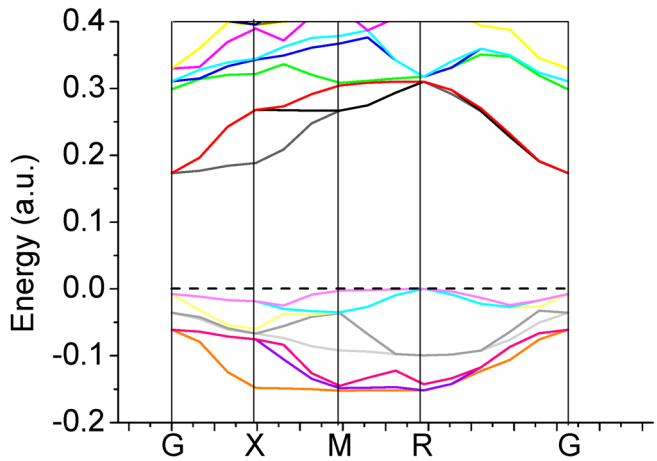

Figure 13. Our hybrid B3PW computed bulk electronic band structure for BZO [75] perovskite.

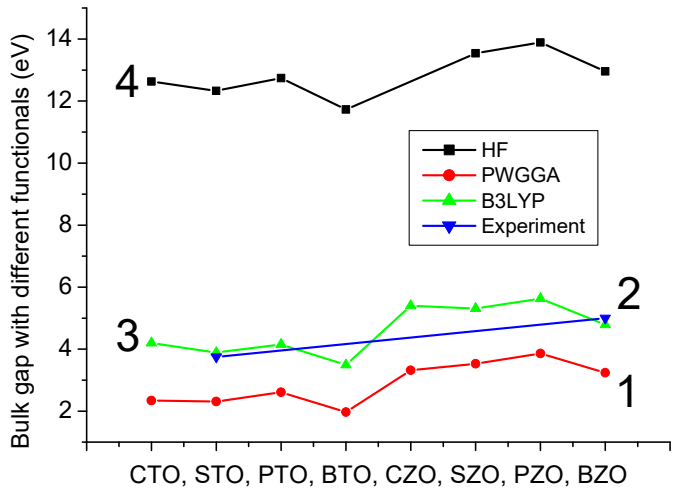

Figure 14. Our computed as well as experimentally measured bulk band gaps at Γ-point for 8 ABO_3 perovskites obtained using different functionals: (1) PWGGA, (2) experimental data, (3) B3LYP and (4) HF.

3.2. ABO_3 Perovskite (001) Surface Atomic and Electronic Structure

Our hybrid exchange–correlation functional B3LYP or B3PW computation results for the (001) surface atomic relaxations for BO_2- as well as AO-terminated ABO_3-type perovskite upper three or two (001) surface layers are recorded in Tables 4 and 5.

Table 4. B3LYP or B3PW computed relaxations of atoms (% of a_0) for the AO-terminated (001) surfaces of eight ABO_3 perovskites [1–3,75,82,94,120].

ABO_3 Perovsk.		**BTO**	**CTO**	**PTO**	**STO**	**BZO**	**CZO**	**PZO**	**SZO**
Termin., (001)		**AO**	**AO**	**AO**	**AO**	**AO**	**AO**	**AO**	**AO**
Layer	**Ion**	**B3PW**	**B3PW**	**B3PW**	**B3PW**	**B3PW**	**B3LYP**	**B3LYP**	**B3LYP**
1	A	−1.99	−8.31	−3.82	−4.84	−4.30	−10.01	−5.69	−7.63
	O	−0.63	−0.42	−0.31	+0.84	−1.23	−0.79	−2.37	−0.86
2	B	+1.74	+1.12	+3.07	+1.75	+0.47	+1.11	+0.57	+0.86
	O	+1.40	+0.01	+2.30	+0.77	+0.18	+0.01	+0.09	−0.05
3	A	-	-	-	-	−0.01	−2.60	−0.47	−1.53
	O	-	-	-	-	−0.14	−0.48	−0.47	−0.45

Table 5. B3LYP or B3PW computed relaxations of atoms (% of a_0) for the BO_2-terminated (001) surfaces of eight ABO_3 perovskites [1–3,75,82,94,120].

ABO_3 Perovsk.		**BTO**	**CTO**	**PTO**	**STO**	**BZO**	**CZO**	**PZO**	**SZO**
Termin., (001)		**BO_2**	**BO_2**	**BO_2**	**BO_2**	**BO_2**	**BO_2**	**BO_2**	**BO_2**
Layer	**Ion**	**B3PW**	**B3PW**	**B3PW**	**B3PW**	**B3PW**	**B3LYP**	**B3LYP**	**B3LYP**
1	B	−3.08	−1.71	−2.81	−2.25	−1.79	−1.30	−2.37	−1.38
	O	−0.35	−0.10	+0.31	−0.13	−1.70	−2.31	−1.99	−2.10
2	A	+2.51	+2.75	+5.32	+3.55	+1.94	+4.23	+4.36	+2.81
	O	+0.38	+1.05	+1.28	+0.57	+0.85	+1.25	+1.04	+0.91
3	B	-	-	-	-	−0.03	−0.05	−0.47	−0.04
	O	-	-	-	-	0.00	−0.09	−0.28	−0.05

As it is possible to see from Tables 4 and 5, the atomic relaxation magnitudes of surface metal atoms A or B, for all eight ABO_3 perovskite (001) surface upper two layers, are almost always noticeably larger than that for the respective O atoms (Tables 4 and 5). This leads to a significant surface rumpling s for the upper-surface plane (Table 6). The only two deviations from this systematic trend are the ZrO_2-terminated CZO and SZO (001) surface outermost layers, where the Ca as well as Sr atom inward relaxation magnitudes are smaller than the respective O atom inward relaxation magnitudes (Table 5). The second systematic trend is that for both AO and BO_2 terminations of all eight ABO_3 perovskite (001) surfaces, as a rule, all atoms of the first (upper) surface layer relax inwards towards the ABO_3 perovskite bulk (Tables 4 and 5). At the same time, all atoms of the second surface layer, for both AO and BO_2 (001) surface terminations, relax upwards (Tables 4 and 5). Again, all third-layer atoms, the same as upper-layer atoms, relax inwards, towards the ABO_3 perovskite bulk (Tables 4 and 5). There are only three exceptions to this systematic trend (Tables 4 and 5). Namely, TiO_2-terminated PTO (001) surface upper-layer O atom relaxes upwards by +0.31% of a_0 (Table 5); SrO-terminated STO (001) surface upper-layer O atom relaxes upwards by +0.84% of a_0, whereas the second-layer O atom on the SrO-terminated $SrZrO_3$ (001) surface relaxes inwards by a very small relaxation magnitude equal to −0.05% of a_0 (Table 4).

Table 6. B3LYP or B3PW computed as well as experimentally detected surface rumpling s and respective atomic displacements Δd_{12} and Δd_{23} (% of a_0) for the BO_2- and AO-terminated (001) surfaces of eight ABO_3 perovskites.

Material	Method	AO-Terminated (001) Surface			BO_2-Terminated (001) Surface		
		s	Δd_{12}	Δd_{23}	s	Δd_{12}	Δd_{23}
BTO	B3PW [1]	1.37	−3.74	1.74	2.73	−5.59	2.51
	LDA [134]		−2.8	1.1		−3.1	0.9
CTO	B3PW [3]	7.89	−9.43	1.12	1.61	−4.46	2.75
	GGA [135]	0.37	−0.44	0.22	0.13	−0.41	0.33
PTO	B3PW [1]	3.51	6.89	3.07	3.12	−8.13	5.32
	LDA [134]		−4.2	2.6		−4.4	3.1
STO	B3PW [2]	5.66	−6.58	1.75	2.12	−5.79	3.55
	LDA [134]		−3.4	1.2		−3.5	1.6
	LEED [136]	4.1 ± 2	−5 ± 1	2 ± 1	2.1 ± 2	1 ± 1	−1 ± 1
	RHEED [137]	4.1	2.6	1.3	2.6	1.8	1.3
BZO	B3PW [82]	3.07	−4.77	0.48	0.09	−3.73	1.97
CZO	B3LYP [120]	9.22	−11.12	3.71	1.01	−5.53	4.28
PZO	B3LYP [94]	3.32	−6.26	1.04	0.38	−6.73	4.83
SZO	B3LYP [94]	6.77	−8.49	2.39	−0.72	−4.19	2.85
	LDA [138]	7.9	−9.1	3.2	−0.7	−6.1	4.2
	GGA [138]	7.8	−9.3	3.3	0.3	−7.4	4.9

B3PW computed [1–3,134,135] as well as experimental [136,137] results, dealing with ABO_3-type perovskite titanates BTO, CTO, PTO and STO, are collected in Table 6. As we can see from Table 6, our hybrid B3PW computation results [2] for STO (001) surfaces are in fair correspondence with the earlier LDA computation results carried out by Meyer et al. [134]. Namely, both computations, our B3PW [2] as well as those LDA computations performed by Meyer et al. [134], provide the same sign for the changes in interlayer distances Δd_{12} and Δd_{23} [2,134] (Table 6). Moreover, our B3PW computed [2] surface rumplings s for SrO as well as TiO_2-terminated STO (001) surfaces are in fair agreement with the actual LEED [136] as well as RHEED [137] experimental measurements. Nonetheless, our B3PW [2] and LDA [134] computed interlayer distance changes Δd_{12} and Δd_{23} fail to agree with the LEED [136] experimental measurements for the TiO_2-terminated STO (001) surface. It is worth noting that LEED [136] and RHEED [137] (Table 6) experimental measurements fail to agree concerning the sign of Δd_{12} for the SrO-terminated STO (001) surface. Also, for the TiO_2-terminated STO (001) surface, LEED [136] and RHEED [137] experiments disagree regarding the sign of the interlayer distance Δd_{23}. As we can see from Table 6, our B3LYP [94] as well as Wang et al.'s [138] LDA and GGA computed surface rumpling s and relative interlayer displacements Δd_{12} and Δd_{23} for the SrO-terminated SZO (001) surface are in fair agreement with each other. In addition, our B3LYP [94] and Wang et al.'s [138] computed interlayer distances Δd_{12} and Δd_{23} are in good agreement with each other for the ZrO_2-terminated SZO (001) surface. The agreement between our B3LYP [94] and Wang et al.'s [138] LDA computed surface rumpling s for the ZrO_2-terminated SZO (001) surface (−0.72% of a_0 and −0.7% of a_0) is almost perfect. Unfortunately, the surface rumpling s, computed by Wang et al., using the GGA exchange–correlation functional [138] for the ZrO_2-terminated SZO (001) surface has a different sign of +0.3% of a_0 (Table 6).

As we can see from Table 7 and Figure 15, our B3PW or B3LYP computed eight ABO_3-type perovskite (001) surface energies are always around 1 eV. Namely, our largest computed (001) surface energy is for the ZrO_2-terminated $CaZrO_3$ (001) surface (1.33 eV) [120], whereas the smallest is for the TiO_2-terminated $PbTiO_3$ (001) surface (0.74 eV) [1]. The smallest energy difference, according our B3PW computations, is for the $BaZrO_3$ ZrO_2- (1.31 eV) and BaO− (1.30 eV) terminated (001) surfaces [82]. The largest (001) surface

energy difference, according to our B3LYP hybrid exchange–correlation functional computations, is for the $CaZrO_3$ perovskite ZrO_2- (1.33 eV) and CaO− (0.87 eV) terminated (001) surfaces (Table 7 and Figure 10) [120]. It is worth noting that according to the calculation results, the surface energies of the nonpolar BO_2-terminated (001) surface was slightly smaller for the BTO, PTO and PZO perovskites; thus, it is more stable (Table 7 and Figure 15).

Table 7. B3LYP or B3PW computed BO_2- or AO-terminated (001) surface energies (in eV per surface cell) for BTO, CTO, PTO, STO, BZO, CZO, PZO, SZO perovskites.

ABO_3 Perovskite	ABO_3 Perovskite (001) Surface	
Termination, Functional	**BO_2-Terminated**	**AO-Terminated**
BTO [1], B3PW	1.07	1.19
CTO [3], B3PW	1.13	0.94
PTO [1], B3PW	0.74	0.83
STO [2], B3PW	1.23	1.15
BZO [82], B3PW	1.31	1.30
CZO [120], B3LYP	1.33	0.87
PZO [94], B3LYP	0.93	1.00
SZO [94], B3LYP	1.24	1.13

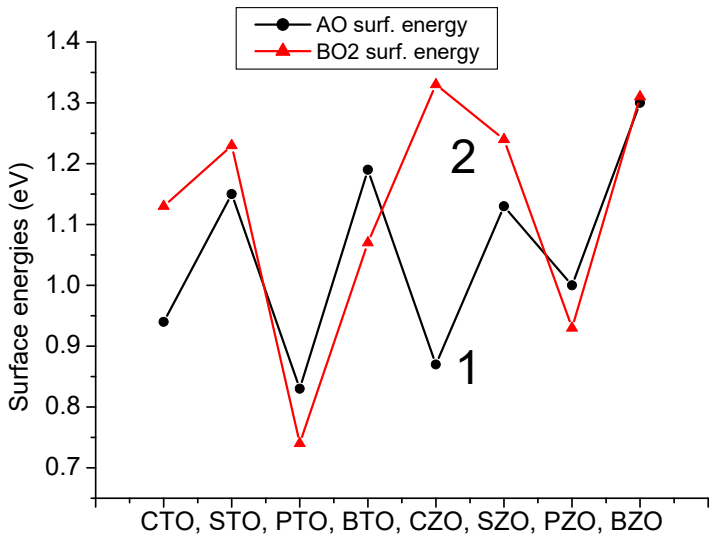

Figure 15. Our B3PW or B3LYP computed AO (1) as well as BO_2-terminated (2) (001) surface energies (in eV per surface cell) for CTO, STO, PTO, BTO, CZO, SZO, PZO and BZO perovskites.

Our B3PW computed electronic bulk band structures for BTO, PTO as well as BZO perovskites are illustrated in Figures 12 and 13. Our B3PW computed TiO_2-terminated electronic (001) surface band structures for BTO and PTO are depicted in Figure 16a,b, whereas the AO-terminated BTO and PTO (001) surfaces are depicted in Figure 17a,b. Our B3PW computed electronic band structures for BaO- (a) and ZrO_2- (b) terminated BZO (001) surfaces are illustrated in Figure 18. Our computed Γ-Γ band gap numerical values for all eight of our computed ABO_3 perovskite bulk as well as their BO_2- and AO-terminated (001) surfaces are collected in Table 8. As we can see from Tables 3 and 8, our B3PW computed STO Γ-Γ bulk band gap (3.96 eV) [114] is in an excellent agreement with the experimentally detected STO bulk Γ-Γ band gap (3.75 eV) [133]. Also, for the BZO perovskite Γ-Γ bulk band gap, the agreement between our B3PW computation result (4.93 eV) [75] and the experiment (5.3 eV) [133] is fine (Tables 3 and 8). The key effect there, as we can see from Table 8 and Figure 19, is that the ABO_3 perovskite bulk Γ-Γ band gap, for all eight of our B3PW or B3LYP computed ABO_3 perovskites, is always reduced near their AO- and BO_2-terminated (001) surfaces. For example, our B3PW computed BZO bulk Γ-Γ band gap

(4.93 eV) (Figure 8) is reduced near the BZO ZrO_2-terminated (001) surface (4.48 eV) as well as near the AO-terminated BZO (001) surface (4.82 eV) (Table 8 and Figures 18 and 19). Also, for all of our other eight computed ABO_3 perovskites, the situation is similar, regarding the reduction of the ABO_3 perovskite bulk Γ-Γ band gap near their (001) surfaces (Figure 14 and Table 8). For example, our B3PW computed BTO bulk Γ-Γ band gap (Figure 12a) (3.55 eV) (Table 8) is also reduced near the BaO-terminated BTO (001) surface (3.49 eV) (Figure 17a) and TiO_2-terminated BTO (001) surface (2.96 eV) (Figures 16a and 19).

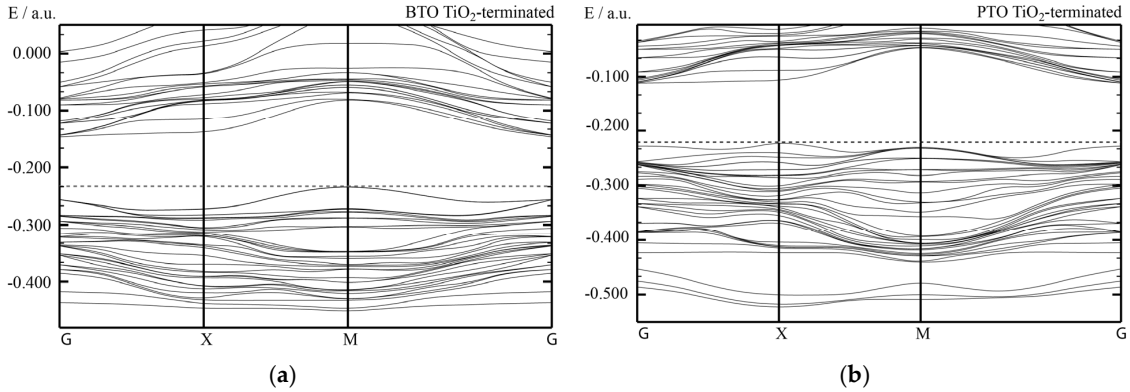

(**a**) (**b**)

Figure 16. Our B3PW simulated electronic band structure for TiO_2-terminated ABO_3 perovskite (001) surfaces of (**a**) BTO and (**b**) PTO.

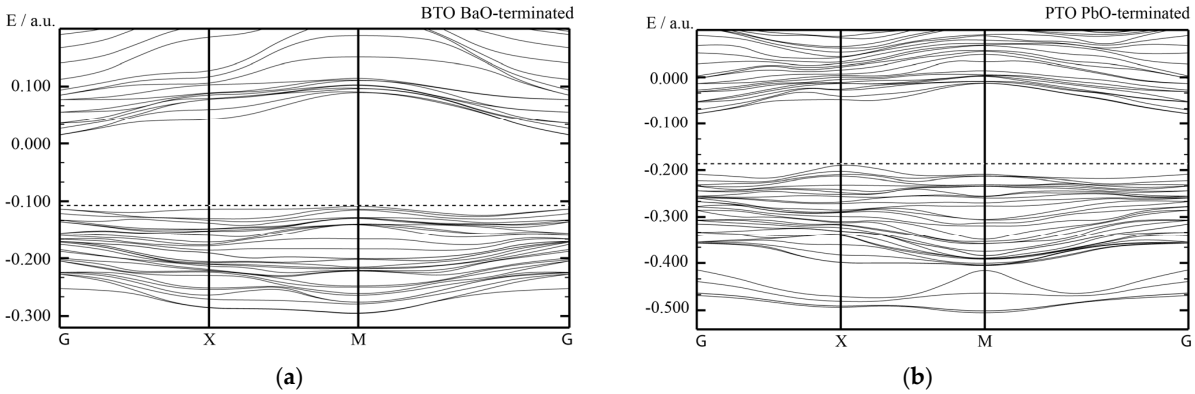

(**a**) (**b**)

Figure 17. Our B3PW simulated electronic band structures for AO-terminated ABO_3 perovskite (001) surfaces of (**a**) BTO and (**b**) PTO.

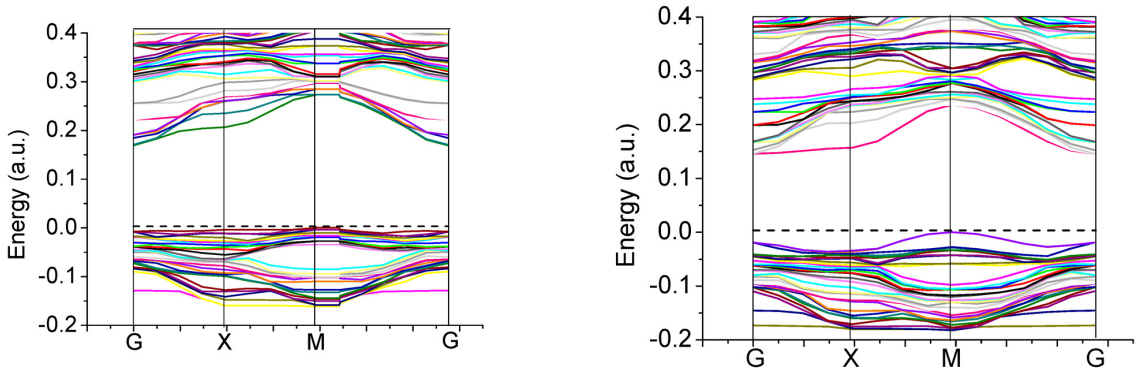

(**a**) (**b**)

Figure 18. Our B3PW simulated electronic band structures for BaO- (**a**) as well as ZrO_2-terminated (**b**) $BaZrO_3$ (001) surfaces.

Table 8. B3PW, B3LYP, PWGGA or HF computed Γ-Γ band gaps for eight ABO_3 perovskite bulk as well as their BO_2- and AO-terminated (001) surfaces (in eV).

Perovskite, Method	Γ-Γ Band Gap, Bulk	BO_2-Termin., (001)	AO-Termin., (001)
BTO, B3PW	3.55 [114]	2.96	3.49
CTO, B3PW	4.18 [75]	3.30	3.87
CTO, B3LYP	4.20 [99]	3.33	3.88
CTO, PWGGA	2.34 [75]	2.06	2.19
CTO, HF	12.63 [75]	11.86	12.53
PTO, B3PW	4.32 [114]	3.18	3.58
STO, B3PW	3.96 [114]	3.95	3.72
BZO, B3PW	4.93 [75]	4.48	4.82
BZO, B3LYP	4.79 [107]	4.37	4.71
BZO, PWGGA	3.24 [75]	2.76	3.08
BZO, HF	12.96 [75]	12.62	12.84
CZO, B3LYP	5.40 [120]	5.22	5.00
PZO, B3LYP	5.63 [94]	4.60	3.86
SZO, B3PW	5.30 [75]	4.98	5.01
SZO, B3LYP	5.31 [94]	4.91	5.04
SZO, PWGGA	3.53 [75]	3.17	3.20
SZO, HF	13.54 [75]	13.19	13.25

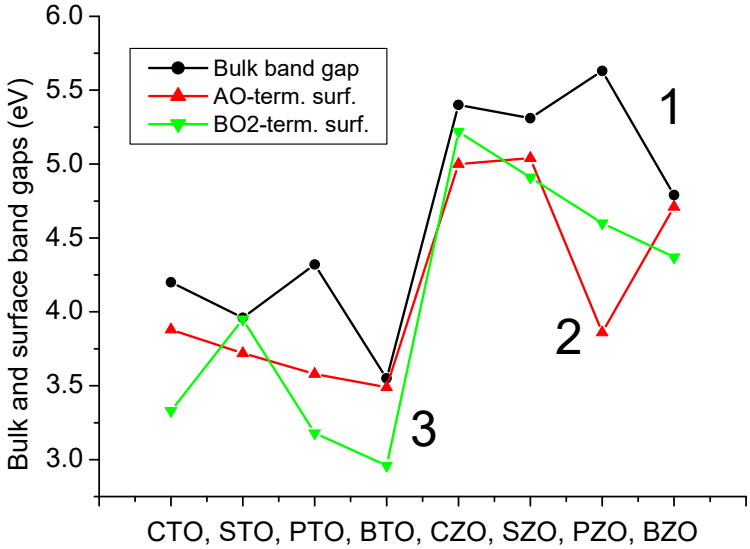

Figure 19. Our computed bulk (1) and AO- (2) as well as BO_2-terminated (3) (001) surface Γ-Γ electronic band gaps for 8 ABO_3 perovskites by means of B3LYP or B3PW functionals.

As we can see from Table 9 and Figure 20, for all eight of our B3LYP or B3PW computed ABO_3 perovskites, we can observe the significant increase in the B-O chemical bond covalency near their BO_2-terminated (001) surfaces, in comparison with bulk. For example, the largest Ti-O chemical bond population increase by 0.30*e*, according to our B3PW computations, is observed for the CTO and STO perovskites, namely, from 0.084*e* and 0.088*e*, respectively, for their bulk to 0.114*e* and 0.118*e*, respectively, near their TiO_2-terminated (001) surfaces [2,3]. Just opposite, the smallest B-O chemical bond population increase is observed for the $PbZrO_3$ perovskite [94]. Namely, the $PbZrO_3$ perovskite Zr-O chemical bond population increased from 0.106*e* (bulk case) to 0.116*e* near the ZrO_2-terminated $PbZrO_3$ (001) surface [94] (Table 9 and Figure 20).

Table 9. B3LYP or B3PW computed B-O bond populations for eight ABO_3 perovskites bulk and also for their BO_2-terminated (001) surfaces (in *e*).

Perovskite	Functional	B-O Chemical Bond Populations	
		ABO_3, Bulk	Surface, (001)
BTO	B3PW	0.098	0.126
CTO	B3PW	0.084	0.114
PTO	B3PW	0.098	0.114
STO	B3PW	0.088	0.118
BZO	B3PW	0.108	0.132
CZO	B3LYP	0.086	0.102
PZO	B3LYP	0.106	0.116
SZO	B3LYP	0.092	0.114

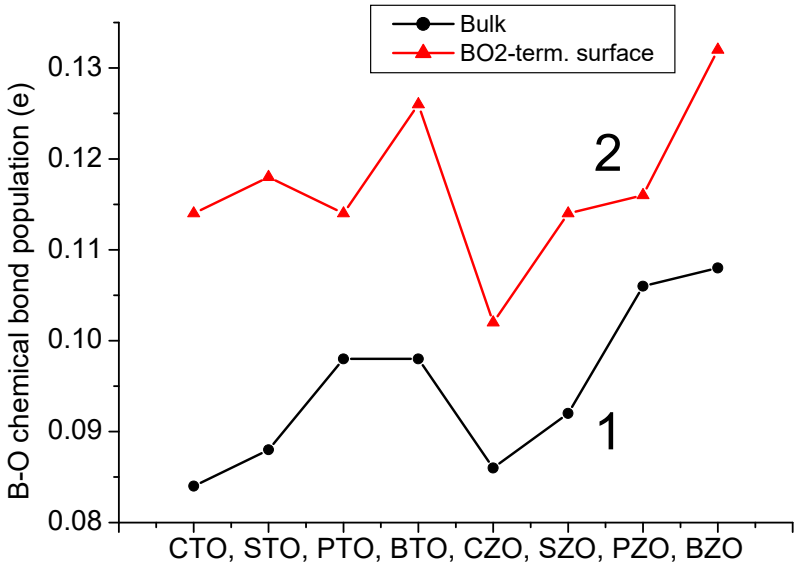

Figure 20. Our B3PW or B3LYP computed bulk (1) as well as BO_2-terminated (2) (001) surface B-O bond populations for BTO, CTO, PTO, STO, BZO, CZO, PZO and SZO perovskites.

3.3. ABO_3 Perovskite (011) Surface Atomic and Electronic Structure

As we can see from Table 10 and Figure 21, for all eight of our B3LYP or B3PW computed ABO_3 perovskites, the systematic tendency is that for all three of their BO-, A- and O-terminated (011) surfaces, all upper-layer atoms relax inwards. The only exception to this systematic trend is upward relaxation of BO-terminated (011) surface upper-layer O atoms for all eight of our computed ABO_3 perovskites (Table 10 and Figure 21).

Table 10. B3PW or B3LYP computed upper-layer atom shifts for 8 ABO_3 perovskite BO-, A- and O-terminated (011) surfaces.

Term. (011)	Atom	CTO	STO	PTO	BTO	CZO	SZO	PZO	BZO
Method		B3PW	B3PW	B3PW	B3PW	B3LYP	B3LYP	B3LYP	B3PW
BO	B	−7.14	−7.69	−8.13	−7.86	−6.06	−6.16	−6.87	−6.61
	O	+4.67	+3.59	+3.30	+2.61	+4.96	+4.36	+4.27	+3.35
A	A	−16.05	−12.81	−11.94	−8.67	−18.67	−15.73	−15.17	−11.81
O	O	−6.10	−6.61	−7.37	−5.40	−5.97	−6.56	−6.61	−7.32

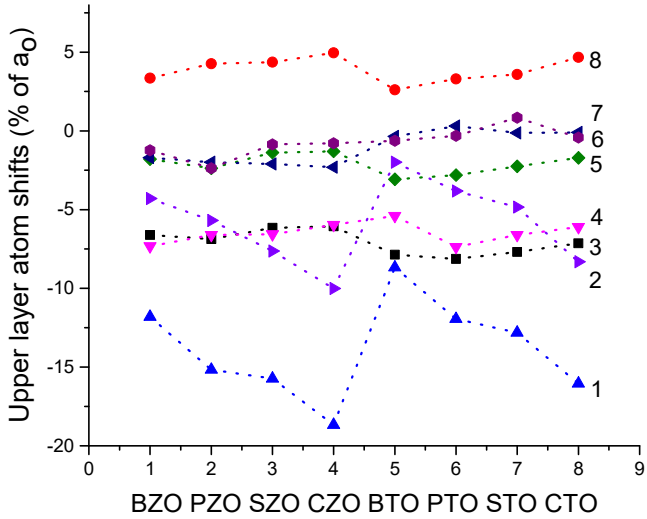

Figure 21. Our computed upper-layer atom shifts for 8 ABO_3 perovskite BO-, A- and O-terminated (011) and also AO- and BO_2-terminated (001) surfaces. Line 1, A-term. (011) surface A atom relaxation. Line 2, AO-term. (001) surface, A atom. Line 3, BO-term. (011) surface, B atom. Line 4, O-terminated (011) surface. Line 5, BO_2-terminated (001) surface, B atom. Line 6, AO-term. (001) surface, O atom relaxation. Line 7, BO_2-term. (001) surface, O atom relaxation. Line 8, BO-terminated (011) surface, O atom relaxation.

It is worth noting that the biggest relaxation magnitude between all upper-layer ABO_3 perovskite (011) surface atoms, for all three possible (011) surface terminations, demonstrates the Ca-terminated surface Ca atom shifting inwards by −18.67% of a_0 (Table 10 and Figure 16) [10]. It is around three times bigger than the displacement magnitudes for the Zr atom (+6.06% of a_0) on the ZrO-terminated as well as O atom (+5.97% of a_0) on the O-terminated CZO (011) surfaces (Table 10 and Figure 21).

As we can see from Table 11 and Figure 22, all our B3LYP computed second-layer O-, Ca- and ZrO-terminated CZO (011) surface atoms relax upwards. The only exception to this systematic trend is the second-layer O atom on the ZrO-terminated CZO (011) surface, which relax inwards (Table 11 and Figure 22). It is worth noting that such systematic trend, mainly upward shift of the second-layer atoms on the A-, O- and BO-terminated (011) surfaces, is quite common for all eight of our computed ABO_3 perovskites (Table 11 and Figure 22). Namely, according to our B3PW or B3LYP computations for eight ABO_3 perovskite (011) surface, all second-layer atoms, located on three different (011) terminations, shift upwards 23 atoms, but relax inwards only 17 atoms (Figure 22 and Table 11).

Table 11. B3PW or B3LYP computed second-layer atom shifts for 8 ABO_3 perovskite BO-, A- and O-terminated (011) surfaces.

Term. (011)	Atom	CTO	STO	PTO	BTO	CZO	SZO	PZO	BZO
Method		B3PW	B3PW	B3PW	B3PW	B3LYP	B3LYP	B3LYP	B3PW
BO	O	−0.44	−0.51	−0.41	−1.02	−0.38	−0.38	−0.24	−0.29
A	O	+1.35	+1.02	−0.61	+0.80	+1.25	+1.24	−0.57	+0.66
O	B	−0.26	−1.02	+0.20	−0.15	+0.75	+1.45	+0.73	+0.12
	A	−2.10	−1.18	+0.18	+1.54	+1.78	−1.43	+0.73	+0.21
	O	+3.43	+1.79	+0.51	+1.95	+0.67	+4.29	+4.29	−0.78

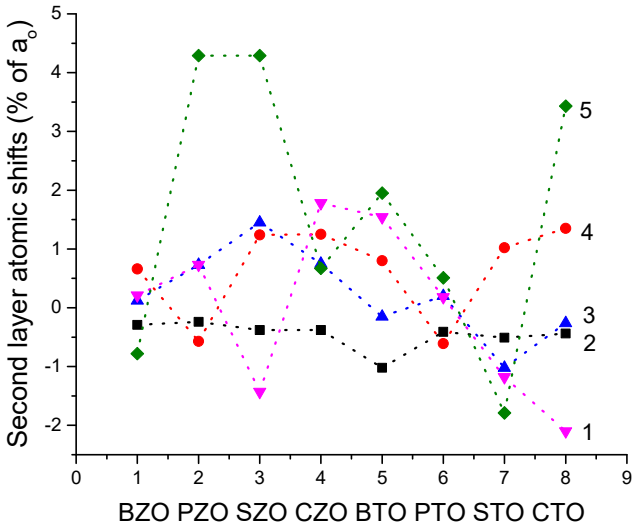

Figure 22. Our B3PW or B3LYP computed second-layer atom relaxation magnitudes. Line 1-our computed O-term. (011) surface A atom shifts. Line 2-BO-term. (011) surface O atom shifts. Line 3-O-term. (011) surface B atom shifts. Line 4-A-term. (011) surface O atom shifts. Line 5-O-term. (011) surface O atom shifts.

As we can see from Table 12 and Figure 23, our B3LYP or B3PW computed ABO_3 perovskite A-, O- or BO-terminated polar (011) surface energies are always larger than the ABO_3 perovskite neutral BO_2- or AO-terminated (001) surface energies. According to our B3LYP computations, the largest ABO_3 perovskite (011) surface energy is for the ZrO-terminated SZO (011) surface (3.61 eV) (Figure 23 and Table 12). The smallest surface energy between all BO-terminated ABO_3 perovskite (011) surfaces is for the TiO-terminated PTO (011) surface, only 1.36 eV. This energy (1.36 eV) is only slightly larger than the ZrO_2-terminated $CaZrO_3$ (001) surface energy (1.33 eV). Nevertheless, according to our B3PW or B3LYP computations, the BO-, O- or A-terminated polar ABO_3 perovskite (011) surface energies are always larger than the neutral BO_2- or AO-terminated ABO_3 perovskite (001) surface energies (Figure 19 and Table 12).

Table 12. B3PW or B3LYP computed (011) and (001) surface energies for CTO, STO, PTO, BTO, CZO, SZO, PZO and BZO perovskites (in eV per surface cell).

Term.	E_{surf}	CTO	STO	PTO	BTO	CZO	SZO	PZO	BZO
Method		B3PW	B3PW	B3PW	B3PW	B3LYP	B3LYP	B3LYP	B3PW
BO	(011)	3.13	3.06	1.36	2.04	3.46	3.61	1.89	3.09
A	(011)	1.91	2.66	2.03	3.24	1.49	2.21	1.74	2.90
O	(011)	1.86	2.04	1.72	1.72	2.08	2.23	1.85	2.32
BO_2	(001)	1.13	1.23	0.74	1.07	1.33	1.24	0.93	1.31
AO	(001)	0.94	1.15	0.83	1.19	0.87	1.13	1.00	1.30

As it is possible to see from Table 13 and Figure 24, according to our B3LYP or B3PW computation results for eight ABO_3 perovskites, the B-O chemical bond population is the smallest for the ABO_3 perovskite bulk. The B-O chemical bond population is increased near the BO_2-terminated (001) surface regarding the bulk value and is in the range of +0.102*e* for the CZO perovskite to 0.132*e* for the BZO perovskite. An even larger B-O chemical bond population is near the BO-terminated (011) ABO_3 perovskite surface. Namely, the plane B(I)-O(I) chemical bond population for all eight of our computed ABO_3 perovskites is in the range of 0.128*e* for the CTO perovskite to 0.152*e* for the BZO perovskite (Table 13 and Figure 24). Finally, as we can see from Table 13 and Figure 24, the ultimately largest B-O chemical bond population, according to our B3LYP or B3PW computations for eight ABO_3 perovskites, is for the BO-terminated (011) surface B(I)-O(II) chemical bond population, in

the direction perpendicular to the BO-terminated (011) surface. It is in the range of 0.186*e* for the CTO perovskite to 0.252*e* for the PZO and BZO perovskites (Figure 24 and Table 13).

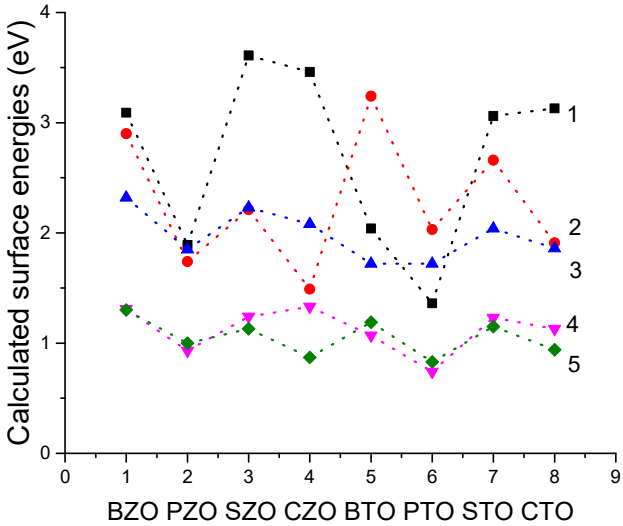

Figure 23. Our B3LYP or B3PW computed ABO_3 surface energies (in eV) for BO- (1), A- (2), O-terminated (3) (011) and also BO_2- (4) and AO-terminated (5) (001) surfaces.

Table 13. B3LYP or B3PW computed 8 ABO_3 perovskite bulk, BO_2-terminated (001) surface and BO-terminated (011) surface B-O chemical bond populations in the plane (B(I)-O(I)) as well as in the direction perpendicular to the (011) surface (B(I)-O(II)).

Chemical bond	CZO	CTO	STO	PTO	BTO	SZO	PZO	BZO
Method	**B3LYP**	**B3PW**	**B3PW**	**B3PW**	**B3PW**	**B3LYP**	**B3LYP**	**B3PW**
Bulk (B-O)	0.086	0.084	0.088	0.098	0.098	0.092	0.106	0.108
(B-O), (001)	0.102	0.114	0.118	0.114	0.126	0.114	0.116	0.132
B(I)-O(I), (011)	0.138	0.128	0.130	0.132	0.130	0.142	0.148	0.152
B(I)-O(II), (011)	0.240	0.186	0.188	0.196	0.198	0.246	0.252	0.252

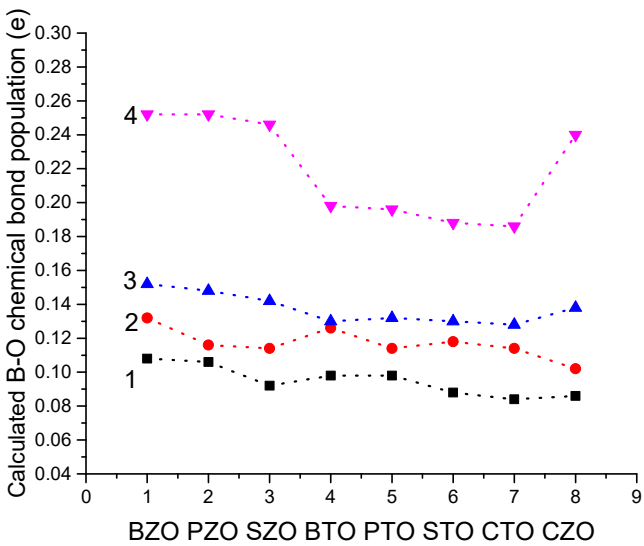

Figure 24. Our B3LYP or B3PW computed B-O chemical bond populations for ABO_3 perovskite bulk (1), BO_2-terminated (001) surfaces (2), as well as for BO-terminated (011) surfaces, B(I)-O(I) (3) and B(I)-O(II) (4).

3.4. ABO_3 Perovskite (111) Surface Atomic and Electronic Structure

As it is possible to see from Table 14, according to our B3LYP computation results for seven ABO_3 perovskites, all atoms on the B-terminated ABO_3 perovskite (111) surface relax inwards. The upper-layer B atom relaxation magnitudes (Table 14) are rather strong, ranging from −3.58% of a_0 for the STO perovskite to −11.19% of a_0 for the BTO perovskite. It is worth noting that almost all second-layer A atoms on the B-terminated ABO_3 perovskite (111) surface relax inwards. In general, they exhibit very large relaxation magnitudes, for example, −14.02% of a_0 for the second-layer Ca atom on the Ti-terminated $CaTiO_3$ (111) surface (Table 14). As we can see from Table 15, according to our B3LYP computations, most of AO_3-terminated ABO_3 perovskite upper-layer atoms also relax inwards. Nevertheless, their relaxation magnitudes are considerably smaller than for the upper-layer atom inward relaxation magnitudes on the B-terminated ABO_3 perovskite upper layer (Tables 14 and 15).

Table 14. B3LYP computed eight ABO_3 perovskite B-terminated (111) surface three upper-layer atom relaxation (% of a_0).

Layer	Ion	BTO	CTO	PTO	STO	BZO	CZO	PZO	SZO
1	B	−11.19	−6.23	−7.57	−3.58	−8.03	−11.07	−9.24	−5.72
2	A	−6.22	−14.02	−10.09	−11.24	−9.73	−11.31	+5.92	−11.92
	O	+2.74	+1.30	−0.13	+1.53	+0.78	+0.14	+2.61	+0.79
3	B	−0.25	−0.26	+0.53	+0.26	−0.02	−0.96	−2.73	+1.53

Table 15. B3LYP computed eight ABO_3 perovskite AO_3-terminated (111) surface three upper-layer atom relaxation (% of a_0).

Layer	Ion	BTO	CTO	PTO	STO	BZO	CZO	PZO	SZO
1	A	−1.24	−0.52	+1.01	+1.33	+1.70	−3.61	−0.05	−0.74
	O	−3.98	−0.81	−2.52	−0.03	−0.57	−0.07	−1.26	−0.52
2	B	+2.49	+2.13	+0.02	+1.81	+0.21	+1.20	+1.18	+0.74
3	A	+1.49	+2.60	+1.26	−0.03	+0.71	−0.02	−0.02	−0.02
	O	−0.25	−0.07	+1.26	−0.26	−0.01	−0.07	−0.02	−0.18

As it is possible to see from Table 16, according to our B3LYP computation results for seven ABO_3 perovskites, the B-terminated ABO_3 perovskite (111) surface energies are always smaller than the respective AO_3-terminated ABO_3 perovskite (111) surface energies. The B-terminated ABO_3 perovskite (111) surface energies (Table 16) are in the energy range of 4.18 eV for the Ti-terminated $CaTiO_3$ (111) surface to 8.19 eV for the Zr-terminated $CaZrO_3$ (111) surface. The AO_3-terminated ABO_3 perovskite (111) surface energies are in the range of 5.86 eV for the CaO_3-terminated $CaTiO_3$ (111) surface to 9.62 eV for the CaO_3-terminated $CaZrO_3$ (111) surface (Table 16).

Table 16. B3LYP computed surface energies for B as well as AO_3-terminated ABO_3 perovskite (111) surfaces (in eV per surface cell).

Termination	BTO	CTO	PTO	STO	BZO	CZO	PZO	SZO
B-terminated	7.28	4.18	6.14	4.99	7.94	8.19	6.93	7.98
AO_3-terminated	8.40	5.86	8.11	6.30	9.33	9.62	8.21	9.45

4. Conclusions

We performed B3PW and B3LYP computations for BTO, CTO, PTO, STO, BZO, CZO, PZO and SZO perovskite neutral (001) along with polar (011) and (111) surfaces. For the neutral AO- as well as BO_2-terminated (001) surfaces, in most cases, all upper-layer atoms relax inwards, although the second-layer atoms shift outwards. There are only

three exceptions to this systematic trend (Tables 4 and 5). Namely, upward relaxation of TiO_2-terminated PTO (001) surface upper-layer O atom by (+0.31% of a_0) (Table 5). On the (001) BO_2-terminated surface, the second-layer metal atoms, as a rule, exhibit larger atomic relaxations than the second-layer O atoms. For most ABO_3 perovskites, the (001) surface rumpling s is bigger for the AO- than BO_2-terminated surfaces. In contrast, the surface energies, for both (001) terminations, are practically identical. Nevertheless, for the BTO, PTO and PZO perovskites, the BO_2-terminated (001) surface has a slightly smaller surface energy, and therefore, it is more stable. In contrast, for CTO, STO, CZO and SZO perovskites, the AO-terminated (001) surface has a slightly smaller surface energy, and therefore, it is slightly more stable. Conversely, different (011) surface terminations exhibit quite different surface energies for the O-terminated, A-terminated, and BO-terminated surfaces. Our computed ABO_3 perovskite (111) surface energies are always significantly larger than the neutral (001) and polar (011) surface energies. Our computed ABO_3 perovskite bulk B-O chemical bond covalency increase near their neutral (001) and especially polar (011) surfaces. It is worth noting that for the (011) surfaces, in the plane B(I)-O(I) chemical bond population for all eight of our computed ABO_3 perovskites is in the range of 0.128e for the CTO perovskite to 0.152e for the BZO perovskite (Table 13 and Figure 24). Finally, as we can see from Table 13 and Figure 24, the ultimately largest B-O chemical bond population, according to our B3LYP or B3PW computations for eight ABO_3 perovskites, is for the BO-terminated (011) surface B(I)-O(II) chemical bond population, in the direction perpendicular to the BO-terminated (011) surface. It is in the range of 0.186e for the CTO perovskite to 0.252e for the PZO and BZO perovskites (Figure 24 and Table 13).

Author Contributions: Formal analysis, R.J.; investigation, R.J. and R.I.E.; writing—original draft preparation, R.I.E. and R.J.; writing—review and editing, R.I.E.; supervision, R.I.E.; project administration, R.I.E. and R.J.; funding acquisition, R.I.E. and R.J. All authors have read and agreed to the published version of the manuscript.

Funding: This study was funded by the Latvian Council of Science Grant Number: LZP-2021/1-464. The Institute of Solid State Physics, University of Latvia (Latvia), as the Centre of Excellence, has received funding from the European Union's Horizon 2020 Framework Programme H2020-WIDESPREAD01-2016-2017-Teaming Phase2 under Grant Agreement No. 739508, project CAMART-2.

Data Availability Statement: Data are contained within the article.

Conflicts of Interest: The authors declare no conflict of interest.

References

1. Eglitis, R.I.; Vanderbilt, D. Ab initio calculations of $BaTiO_3$ and $PbTiO_3$ (001) and (011) surface structures. *Phys. Rev. B* **2007**, *76*, 155439. [CrossRef]
2. Eglitis, R.I.; Vanderbilt, D. First-principles calculations of atomic and electronic structure of $SrTiO_3$ (001) and (011) surfaces. *Phys. Rev. B* **2008**, *77*, 195408. [CrossRef]
3. Eglitis, R.I.; Vanderbilt, D. Ab initio calculations of the atomic and electronic structure of $CaTiO_3$ (001) and (011) surfaces. *Phys. Rev. B* **2008**, *78*, 155420. [CrossRef]
4. Dawber, M.; Rabe, K.M.; Scott, J.F. Physics of thin-film ferroelectric oxides. *Rev. Mod. Phys.* **2005**, *77*, 1083–1130. [CrossRef]
5. Eglitis, R.I. Ab initio hybrid DFT calculations of $BaTiO_3$, $PbTiO_3$, $SrZrO_3$ and $PbZrO_3$ (111) surfaces. *Appl. Surf. Sci.* **2015**, *358*, 556–562. [CrossRef]
6. Erdman, N.; Poeppelmeier, K.R.; Asta, M.; Warschkov, O.; Ellis, D.E.; Marks, L.D. The structure and chemistry of the TiO_2-rich surface of $SrTiO_3$ (001). *Nature* **2002**, *419*, 55–58. [CrossRef]
7. Celik, F.A. Electronic structure of two-dimensional-layered $PbTiO_3$ perovskite crystal: An extended tight-binding study based on DFT. *Bull. Mater. Sci.* **2022**, *45*, 108. [CrossRef]
8. Wang, J.L.; Vilquin, B.; Barrett, N. Screening of ferroelectric domains on $BaTiO_3$ (001) surface by ultraviolet photo-induced charge and dissociative water adsorption. *Appl. Phys. Lett.* **2012**, *101*, 092902. [CrossRef]
9. Li, W.; Landis, C.M.; Demkov, A. Domain morphology and electro-optic effect in Si-integrated epitaxial $BaTiO_3$ films. *Phys. Rev. Mater.* **2022**, *6*, 095203. [CrossRef]
10. Eglitis, R.I.; Kleperis, J.; Purans, J.; Popov, A.I.; Jia, R. Ab initio calculations of $CaZrO_3$ (011) surfaces: Systematic trends in polar (011) surface calculations of ABO_3 perovskites. *J. Mater. Sci.* **2020**, *55*, 203–217. [CrossRef]

11. Costa-Amaral, R.; Gohda, Y. First-principles study of the adsorption of 3d transition metals on BaO- and TiO_2-terminated cubic-phase $BaTiO_3$ (001) surfaces. *J. Chem. Phys.* **2020**, *152*, 204701. [CrossRef]
12. Lyu, J.; Fina, I.; Solanas, R.; Fontcuberta, J.; Sanchez, F. Tailoring lattice strain and Ferroelectric Polarization of Epitaxial $BaTiO_3$ Thin Films on Si (001). *Sci. Rep.* **2018**, *8*, 495. [CrossRef]
13. Ellinger, F.; Shafiq, M.; Ahmad, I.; Reticcioli, M.; Franchini, C. Small polaron formation on the Nb-doped $SrTiO_3$ (001) surface. *Phys. Rev. Mater.* **2023**, *7*, 064602. [CrossRef]
14. Wang, Y.; Zhang, Z.; Wang, Y.; Doan, E.; Yuan, L.; Tang, W.; Yang, K. First-principles investigation of structural, electronic, and energetic properties of $BaSnO_3$ (001) surfaces. *Vacuum* **2023**, *212*, 111977. [CrossRef]
15. Abbasi, P.; Fenning, D.P.; Pascal, T.A. Investigation of local distortion effects on X-ray absorption of ferroelectric perovskites from first principles simulations. *Nanoscale* **2023**, *15*, 5193–5200. [CrossRef] [PubMed]
16. Barret, N.; Dionot, J.; Martinotti, D.; Salje, E.K.H.; Mathieu, C. Evidence of surface anomaly during the cubic-tetragonal phase transition in $BaTiO_3$ (001). *Appl. Phys. Lett.* **2018**, *113*, 022901. [CrossRef]
17. Franchini, C.; Reticcioli, M.; Setvin, M.; Diebold, U. Polarons in materials. *Nat. Rev. Mater.* **2021**, *6*, 560–586. [CrossRef]
18. Chen, P.; Xu, Y.; Wang, N.; Oganov, A.R.; Duan, W. Effects of ferroelectric polarization on surface phase diagram: Evolutionary algorithm study of the $BaTiO_3$ (001) surface. *Phys. Rev. B* **2015**, *92*, 085432. [CrossRef]
19. Brivio, S.; Petti, D.; Bertacco, R.; Cezar, J.C. Electric field control of magnetic anisotropies and magnetic coercivity in Fe/$BaTiO_3$ (001) heterostructures. *Appl. Phys. Lett.* **2011**, *98*, 092505. [CrossRef]
20. Gao, H.; Liu, X.; Yue, Z.; Liu, Y.; Lin, T. First-principles study on strain-controllable magnetoelectric coupling behavior of two-dimensional $BaTiO_3$ (001) ultrathin film with surface Ba vacancy. *Ceram. Int.* **2020**, *46*, 24682–24688. [CrossRef]
21. Saghayezhian, M.; Sani, S.M.R.; Zhang, J.; Plummer, E.W. Rumpling and enhanced covalency at the $SrTiO_3$ (001) surface. *J. Phys. Chem. C* **2019**, *123*, 8086–8091. [CrossRef]
22. Hamazaki, Y.; Gohda, Y. Enhancement of magnetoelectric coupling by insertion of Co atomic layer into Fe_3Si/$BaTiO_3$ (001) interfaces identified by first-principles calculations. *J. Appl. Phys.* **2019**, *126*, 233902. [CrossRef]
23. Sambrano, J.R.; Longo, V.M.; Longo, E.; Taft, C.A. Electronic and structural properties of the (001) $SrZrO_3$ surface. *J. Mol. Struct. THEOCHEM* **2007**, *813*, 49–56. [CrossRef]
24. Setvin, M.; Reticcioli, M.; Poelzleitner, F.; Hulva, J.; Schmid, M.; Boatner, L.A.; Franchini, C.; Diebold, U. Polarity compensation mechanisms on the perovskite surface $KTaO_3$ (001). *Science* **2018**, *359*, 572–575. [CrossRef]
25. Wang, Z.; Hao, X.; Gerhold, S.; Schmid, M.; Franchini, C.; Diebold, U. Vacancy clusters at domain boundaries and band bending at the $SrTiO_3$ (110) surface. *Phys. Rev. B* **2014**, *90*, 035436. [CrossRef]
26. Le, T.T.; Ekerdt, J.G. Epitaxial growth of high-*k* $BaxSr_{1-x}TiO_3$ thin films on $SrTiO_3$ (001) substrates by atomic layer deposition. *J. Vac. Sci. Technol. A* **2020**, *38*, 032401. [CrossRef]
27. Zhong, W.; Vanderbilt, D.; Rabe, K.M. First-principles theory of ferroelectric phase transitions for perovskites: The case of $BaTiO_3$. *Phys. Rev. B* **1995**, *52*, 6301. [CrossRef]
28. Bellaiche, L.; Vanderbilt, D. Virtual crystal approximation revisited: Application to dielectric and piezoelectric properties of perovskites. *Phys. Rev. B* **2000**, *61*, 7877. [CrossRef]
29. Dufour, P.; Maroutian, T.; Vallet, M.; Patel, K.; Chanthbouala, A.; Jacquemont, C.; Yedra, L.; Humbert, V.; Godel, F.; Xu, B.; et al. Ferroelectric phase transitions in epitaxial antiferroelectric $PbZrO_3$ thin films. *Appl. Phys. Rev.* **2023**, *10*, 021405. [CrossRef]
30. Wang, S.; Yan, H.; Zhao, D.; Tan, Z.; Shi, Q. Low temperature heat capacity and thermodynamic function of $BaZrO_3$ and $PbZrO_3$. *J. Chem. Thermodyn.* **2021**, *158*, 106449. [CrossRef]
31. Loureiro, F.J.A.; Nasani, N.; Reddy, G.S.; Munirathnam, N.R.; Fagg, D.P. A review on sintering technology of proton conducting $BaCeO_3$-$BaZrO_3$ perovskite oxide materials for Protonic Ceramic Fuel Cells. *J. Power Sources* **2019**, *438*, 226991. [CrossRef]
32. Gurgel, M.F.C.; Moreira, M.L.; Paris, E.C.; Espinosa, J.W.M.; Pizani, P.S.; Varela, J.A.; Longo, E. $BaZrO_3$ photoluminescence property: An ab initio analysis of structural deformation and symmetry changes. *Int. J. Quantum. Chem.* **2011**, *111*, 694–701. [CrossRef]
33. Kirby, N.M.; van Riessen, A.; Buckley, C.E.; Wittorff, V.W. Oxalate-precursor processing for high quality $BaZrO_3$. *J. Mater. Sci.* **2005**, *40*, 97–106. [CrossRef]
34. Prasatkhetragarn, A.; Sareein, T.; Triamnak, N.; Yimnirun, R. Dielectric and ferroelectric properties of modified-$BaTiO_3$ lead-free ceramics prepared by solid solution method. *Ferroelectrics* **2022**, *586*, 224–241. [CrossRef]
35. Ring, A.E.; Kesson, S.E.; Reeve, K.D.; Levins, D.M.; Ramm, E.J. *Radioactive Waste Forms for the Future*; Lutze, W., Ewings, R.C., Eds.; North-Holland: Amsterdam, The Netherlands, 1987.
36. Scott, J.F.; Paz de Araujo, C.A. Ferroelectric Memories. *Science* **1989**, *246*, 1400–1405. [CrossRef] [PubMed]
37. Scott, J.F. Applications of Modern Ferroelectrics. *Science* **2007**, *315*, 954–959. [CrossRef]
38. Sicron, N.; Ravel, B.; Yacoby, Y.; Stern, E.A.; Dogan, F.; Rehr, J.J. Nature of the ferroelectric phase transition in $PbTiO_3$. *Phys. Rev. B* **1994**, *50*, 13168–13180. [CrossRef]
39. Kisiel, M.; Brovko, O.O.; Yildiz, D.; Pawlak, R.; Gysin, U.; Tosatti, E.; Meyer, E. Mechanical dissipation from charge and spin transitions in oxygen-deficient $SrTiO_3$ surfaces. *Nat. Commun.* **2018**, *9*, 2946. [CrossRef]
40. Goodenough, J.B. Electronic and ionic transport properties and other physical aspects of perovskites. *Rep. Prog. Phys.* **2004**, *67*, 1915–1993. [CrossRef]

41. Santander-Syro, A.F.; Fortuna, F.; Bareille, C.; Rödel, T.C.; Landolt, G.; Plumb, N.C.; Dil, J.H.; Radovič, M. Giant spin splitting of the two-dimensional electron gas at the surface of $SrTiO_3$. *Nat. Mater.* **2014**, *13*, 1085–1090. [CrossRef]
42. Liu, Z.Q.; Lü, W.M.; Lim, S.L.; Qiu, X.P.; Bao, N.N.; Motapothula, M.; Yi, J.B.; Yang, M.; Dhar, S.; Venkatesan, T.; et al. Reversible room-temperature ferromagnetism in Nb-doped $SrTiO_3$ single crystals. *Phys. Rev. B* **2013**, *87*, 220405(R). [CrossRef]
43. Orak, İ.; Karabulat, A.; Yiğit, E.; Sevgili, Ö.; Ruşen, A.; Ozel, F. The diode and photodiode performances of $BaZrO_3$ perovskite-based device under the influence of thermal and light external stimuli. *Sens. Actuators Phys. A* **2022**, *337*, 113413. [CrossRef]
44. Exner, J.; Nazarenus, T.; Kita, J.; Moos, R. Dense Y-doped ion conducting perovskite films of $BaZrO_3$, $BaSnO_3$ and $BaCeO_3$ for SOFC applications produced by powder aerosol deposition at room temperature. *Int. J. Hydrogen Energy* **2020**, *45*, 10000–10016. [CrossRef]
45. Parida, S.; Rout, S.K.; Cavalcante, L.S.; Sinha, E.; Li, M.S.; Subramanian, V.; Gupta, N.; Gupta, V.R.; Varela, J.A.; Longo, E. Structural refinement, optical and microwave dielectric properties of $BaZrO_3$. *Ceram. Int.* **2012**, *38*, 2129–2138. [CrossRef]
46. Davies, R.A.; Islam, M.S.; Gale, J.D. Dopant and Proton Incorporation in Perovskite-Type Zirconates. *Solid State Ion.* **1999**, *126*, 323–335. [CrossRef]
47. Janke, D. Studies Using EMF. Probes of the Continuous Measurement of Dissolved Oxygen in Steel Melts. *Metall. Mater. Trans. B* **1982**, *13B*, 227. [CrossRef]
48. Setiawan, A.H.; Fergus, J.W. Preparation and Characterisation of Indium-Doped Calcium Zirconate for the Electrolyte in Hydrogen Sensors for Use in Molten Aluminium. *Ceram. Trans.* **2002**, *130*, 47–56.
49. Singh, D.J. Structure and energetics of antiferroelectric $PbZrO_3$. *Phys. Rev. B* **1995**, *52*, 12559–12563. [CrossRef]
50. Lin, S.; Xiu, Z.; Liu, J.; Xu, F.; Yu, W.; Yu, J.; Feng, G. Combustion synthesis and characterization of perovskite $SrTiO_3$ nanopowders. *J. Alloys Compd.* **2008**, *457*, L12–L14.
51. Mete, E.; Shaltaf, R.; Ellialtoğlu, S. Electronic and structural properties of a 4d perovskite: Cubic phase of $SrZrO_3$. *Phys. Rev. B* **2003**, *68*, 035119. [CrossRef]
52. Cavalcante, L.S.; Simoes, A.Z.; Sczancovski, J.C.; Longo, V.M.; Erlo, R.; Escoto, M.T.; Longo, E.; Varela, J.A. $SrZrO_3$ powders obtained by chemical method: Synthesis, characterization and optical absorption behavior. *Solid State Sci.* **2007**, *9*, 1020–1027. [CrossRef]
53. Longo, V.M.; Cavalcante, L.S.; Figneiredo, A.T.; Santos, L.P.S.; Longo, E.; Varela, J.A.; Sambrano, J.R.; Paskocimas, C.A.; De Vicente, F.S.; Hernandes, A.C. Highly intense violet-blue light emission at room temperature in structurally disordered $SrZrO_3$ powders. *Appl. Phys. Lett.* **2007**, *90*, 091906. [CrossRef]
54. Eglitis, R.I.; Purans, J.; Popov, A.I.; Bocharov, D.; Chekhovska, A.; Jia, R. Ab initio computations of O and AO as well as ReO_2, WO_2 and BO_2-terminated ReO_3, WO_3, $BaTiO_3$, $SrTiO_3$ and $BaZrO_3$ (001) surfaces. *Symmetry* **2022**, *14*, 1050. [CrossRef]
55. Zhang, R.; Hwang, G.S. First-principles mechanistic study of the initial growth of SrO by atomic layer deposition on TiO_2-terminated $SrTiO_3$ (001). *J. Phys. Chem. C* **2020**, *124*, 28116. [CrossRef]
56. Kasai, M.; Dohi, H. Surface structure and electrochemical properties of platinum films grown on $SrTiO_3$ (100) substrates. *Surf. Sci.* **2017**, *666*, 14–22. [CrossRef]
57. Waldow, S.P.; Souza, R.A.D. Computational study of oxygen diffusion along a [100] dislocations in the perovskite oxide $SrTiO_3$. *ACS Appl. Mater Interfaces* **2016**, *8*, 1224–1256. [CrossRef] [PubMed]
58. Brik, M.G.; Ma, C.G.; Krasnenko, V. First-principles calculations of the structural and electronic properties of the cubic $CaZrO_3$ (001) surfaces. *Surf. Sci.* **2013**, *608*, 146–153. [CrossRef]
59. Zhong, M.; Zeng, W.; Liu, F.S.; Tang, B.; Liu, Q.J. First-principles study of the atomic structures, electronic properties, and surface stability of $BaTiO_3$ (001) and (011) surfaces. *Surf. Interface Anal.* **2019**, *51*, 1021–1032. [CrossRef]
60. Eglitis, R.I. Comparative first-principles calculations of $SrTiO_3$, $BaTiO_3$, $PbTiO_3$ and $CaTiO_3$ (001), (011) and (111) surfaces. *Ferroelectrics* **2015**, *483*, 53–67. [CrossRef]
61. Alam, N.N.; Malik, N.A.; Samat, M.H.; Hussin, N.H.; Jaafar, N.K.; Radzwan, A.; Mohyedin, M.Z.; Haq, B.U.; Ali, A.M.M.; Hassan, O.H.; et al. Underlaying mechanism of surface (001) cubic $ATiO_3$ (A = Pb, Sn) in enhancing thermoelectric performance of thin-film applications using density functional theory. *Surf. Interfaces* **2021**, *27*, 101524. [CrossRef]
62. Zhao, X.; Selloni, A. Structure and stability of $NaTaO_3$ (001) and $KTaO_3$ (001) surfaces. *Phys. Rev. Mater.* **2019**, *3*, 015801. [CrossRef]
63. Kolpak, A.M.; Li, D.; Shao, R.; Rappe, A.M.; Bonnell, D.A. Evolution of the surface structure and thermodynamic stability of the $BaTiO_3$ (001) surface. *Phys. Rev. Lett.* **2008**, *101*, 036102. [CrossRef] [PubMed]
64. Eglitis, R.I.; Piskunov, S. First principles calculations of $SrZrO_3$ bulk and ZrO_2-terminated (001) surface *F* centers. *Comput. Condens. Matter* **2016**, *7*, 1–6. [CrossRef]
65. Sorokine, A.; Bocharov, D.; Piskunov, S.; Kashcheyevs, V. Electronic charge redistribution in $LaAlO_3$ (001) thin films deposited at $SrTiO_3$ substrate: First-principles analysis and the role of stoichiometry. *Phys. Rev. B* **2012**, *86*, 155410. [CrossRef]
66. Krasnenko, V.; Platonenko, A.; Liivand, A.; Rusevich, L.L.; Mastrikov, Y.A.; Zvejnieks, G.; Sokolov, M.; Kotomin, E.A. Modeling of the Lattice Dynamics in Strontium Titanate Films of Various Thicknesses: Raman Scattering Studies. *Materials* **2023**, *16*, 6207. [CrossRef] [PubMed]
67. Piskunov, S.; Eglitis, R.I. First principles hybrid DFT calculations of $BaTiO_3/SrTiO_3$ (001) interface. *Solid State Ion.* **2015**, *274*, 29–33. [CrossRef]
68. Gao, H.; Yue, Z.; Liu, Y.; Hu, J.; Li, X. A first-principles study on the multiferroic property of two-dimensional $BaTiO_3$ (001) ultrathin film with surface Ba vacancy. *Nanomaterials* **2019**, *9*, 269. [CrossRef]

69. Tiano, Y.; Adamo, C.; Schlom, D.G.; Burch, K.S. Optical properties of $SrTiO_3$ on silicon (100). *Appl. Phys. Lett.* **2013**, *102*, 041906. [CrossRef]
70. Hong, M.; Wohlwend, J.L.; Behera, R.K.; Philpott, S.R.; Sinott, S.B.; Uberuaga, B.P. Surface diffusion on $SrTiO_3$ (100): A temperature accelerated dynamics and first principles study. *Surf. Sci.* **2013**, *617*, 237–241. [CrossRef]
71. Iles, N.; Finocchi, F.; Khodja, K.D. A systematic study of ideal and double layer reconstruction of ABO_3 (001) surfaces (A = Sr, Ba:B = Ti, Zr) from first principles. *J. Phys. Condens. Matter* **2010**, *22*, 305001. [CrossRef]
72. Heifets, E.; Dorfman, S.; Fuks, D.; Kotomin, E. Atomistic simulation of the [001] surface structure in $BaTiO_3$. *Thin Solid Film.* **1997**, *296*, 76–78. [CrossRef]
73. Sokolov, M.; Eglitis, R.I.; Piskunov, S.; Zhukovskii, Y.F. Ab initio hybrid DFT calculations of $BaTiO_3$ bulk and BaO-terminated (001) surface F-centers. *Int. J. Mod. Phys. B* **2017**, *31*, 1750251. [CrossRef]
74. Wang, Y.; Zhao, H.; Zhang, L.; Chen, J.; Xing, X. $PbTiO_3$-based perovskite ferroelectric and multiferroic thin films. *Phys. Chem. Chem. Phys.* **2017**, *19*, 17493–17515. [CrossRef] [PubMed]
75. Eglitis, R.I.; Popov, A.I. Systematic trends in (001) surface ab initio calculations of ABO_3 perovskites. *J. Saudi Chem. Soc.* **2018**, *22*, 459–468. [CrossRef]
76. Ohtomo, A.; Hwang, H.K. A high-mobility electron gas at the $LaAlO_3/SrTiO_3$ heterointerface. *Nature* **2004**, *427*, 423–426. [CrossRef] [PubMed]
77. Nishio, K.; Ohnishi, T.; Mitsuishi, K.; Ohta, N.; Watanabe, K.; Takada, K. Orientation alignment of epitaxial $LiCoO_2$ thin films on vicinal $SrTiO_3$ (100) substrates. *J. Power Sources* **2016**, *325*, 306–310. [CrossRef]
78. Rodenbücher, C.; Bihlmayer, G.; Korte, C.; Rytz, D.; Szade, J.; Szot, K. An Operando Study of the Thermal Reduction of $BaTiO_3$ Crystals: The Nature of the Insulator-Metal Transition of the Surface Layer. *Crystals* **2023**, *13*, 1278. [CrossRef]
79. Yuk, S.F.; Asthagiri, A. A first-principles study of Pt thin films on $SrTiO_3$ (100): Support effects on CO adsorption. *J. Chem. Phys.* **2015**, *142*, 124704. [CrossRef]
80. Torres-Torres, D.; Hurtado-Macias, A.; Herrera-Basurto, R.; Conteras, E.; Sánchez, S.; Mercarder-Trejo, F.; González-Hernández, J.; Auciello, O. Anisotropic behavior of mechanical properties for the *a*- and *c*-domains in a (001) $BaTiO_3$ single crystal. *J. Phys. Condens. Matter* **2023**, *35*, 355703. [CrossRef]
81. Cieślik, K.; Wrana, D.; Rogala, M.; Rodenbücher, C.; Szot, K.; Krok, F. The effect of reduction and Oxidation Processes on the Work Function of Metal Oxide Crystals: TiO_2 (110) and $SrTiO_3$ (001) Case. *Crystals* **2023**, *13*, 1052. [CrossRef]
82. Eglitis, R.I. First-principles calculations of $BaZrO_3$ (001) and (011) surfaces. *J. Phys. Condens. Matter* **2007**, *19*, 356004. [CrossRef]
83. Padilla, J.; Vanderbilt, D. Ab initio study of $SrTiO_3$ surfaces. *Surf. Sci.* **1998**, *418*, 64–76. [CrossRef]
84. Huang, R.; Fung, V.; Zhang, Y.; Mullins, D.R.; Wu, Z.; Jiang, D. Understanding Methanol Coupling on $SrTiO_3$ from First Principles. *J. Phys. Chem. C* **2018**, *122*, 7210–7216. [CrossRef]
85. Kotomin, E.A.; Eglitis, R.I.; Maier, J.; Heifets, E. Calculations of the atomic and electronic structure for $SrTiO_3$ perovskite thin films. *Thin Solid Film.* **2001**, *400*, 76–80. [CrossRef]
86. Zhang, G.X.; Xie, Y.; Yu, H.T.; Fu, H.G. First-principles calculations of the stability and electronic properties of the $PbTiO_3$ (110) polar surface. *Comput. Chem.* **2009**, *30*, 1785–1789. [CrossRef] [PubMed]
87. Zhang, J.M.; Pang, Q.; Xu, K.W.; Ji, V. First-principles study of the (110) polar surface of cubic $PbTiO_3$. *Comput. Mater. Sci.* **2009**, *44*, 1360–1365. [CrossRef]
88. Bottin, F.; Finocchi, F.; Noguera, C. Stability and electronic structure of the (1×1) $SrTiO_3$ (110) polar surfaces by first-principles calculations. *Phys. Rev. B* **2003**, *68*, 035418. [CrossRef]
89. Heifets, E.; Goddard, W.A.; Kotomin, E.A.; Eglitis, R.I.; Borstel, G. Ab initio calculations of the $SrTiO_3$ (110) polar surface. *Phys. Rev. B* **2004**, *69*, 035408. [CrossRef]
90. Enterkin, J.A.; Subramanian, A.K.; Russell, B.C.; Castell, M.R.; Poeppelmeier, K.R.; Marks, L.D. A homologous series of structures on the surface of $SrTiO_3$ (110). *Nat. Mater.* **2010**, *9*, 245–248. [CrossRef]
91. Fleischer, K.; Kim, S.; Walls, B.; Zhussupbekov, K.; Shvets, I.V. Optical Anisotropy of $SrTiO_3$ (110) for Different Surface Terminations. *Phys. Status Solidi B* **2018**, *255*, 1700459. [CrossRef]
92. Zhang, J.M.; Cui, J.; Xu, K.W.; Ji, V.; Man, Z.Y. Ab initio modeling of $CaTiO_3$ (110) polar surfaces. *Phys. Rev. B* **2007**, *76*, 115426. [CrossRef]
93. Heifets, E.; Ho, J.; Merinov, B. Density functional simulation of the $BaZrO_3$ (011) surface structure. *Phys. Rev. B* **2007**, *75*, 155431. [CrossRef]
94. Eglitis, R.I.; Rohlfing, M. First-principles calculations of the atomic and electronic structure of $SrZrO_3$ and $PbZrO_3$ (001) and (011) surfaces. *J. Phys. Condens. Matter* **2010**, *22*, 415901. [CrossRef] [PubMed]
95. Chen, H.; Xie, Y.; Zhang, G.X.; Yu, H.T. A first-principles investigation of the stabilities and electronic properties of $SrZrO_3$ (110) (1×1) polar terminations. *J. Phys. Condens. Matter* **2014**, *26*, 395002. [CrossRef] [PubMed]
96. Hagendorf, C.; Schindler, K.M.; Doege, T.; Neddermeyer, H. An STM, XPS and LEED investigation of the $BaTiO_3$ (111) surface. *Surf. Sci.* **1998**, *402–404*, 581–585. [CrossRef]
97. Chun, H.J.; Lee, Y.; Kim, S.; Yoon, Y.; Kim, Y.; Park, S.C. Surface Termination of $BaTiO_3$ (111) Single Crystal: A Combined DFT and XPS Study. *Appl. Surf. Sci.* **2022**, *578*, 152018. [CrossRef]
98. Cohen, R.E. Periodic slab LAPW computations for ferroelectric $BaTiO_3$. *J. Phys. Chem. Solids* **1996**, *57*, 1393–1396. [CrossRef]

99. Eglitis, R.I. Comparative ab initio calculations of $SrTiO_3$ and $CaTiO_3$ polar (111) surfaces. *Phys. Status Solidi B* **2015**, *252*, 635–642. [CrossRef]
100. Haruyama, Y.; Aiura, Y.; Bando, H.; Nishihara, Y.; Kato, H. Annealing temperature dependence on the electronic structure of the reduced $SrTiO_3$ (111) surface. *J. Electron Spectrosc. Relat. Phenom.* **1998**, *88–91*, 695–698. [CrossRef]
101. Pojani, A.; Finocchi, F.; Noguera, C. Polarity on the $SrTiO_3$ (111) and (110) surfaces. *Surf. Sci.* **1999**, *442*, 179–198. [CrossRef]
102. Torrelles, X.; Cantele, G.; Luca, G.M.D.; Capua, R.D.; Drnec, J.; Felici, R.; Ninno, D.; Herranz, G.; Salluzzo, M. Electronic and structural reconstructions of the polar (111) $SrTiO_3$ surface. *Phys. Rev. B* **2019**, *99*, 205421. [CrossRef]
103. Marks, L.D.; Chiaramonti, A.N.; Rahman, S.U.; Castel, M.R. Transition from Order to Configurational Disorder for Surface Reconstructions on $SrTiO_3$ (111). *Phys. Rev. Lett.* **2015**, *114*, 226101. [CrossRef] [PubMed]
104. Pang, Q.; Zhang, J.M.; Xu, K.W.; Ji, V. Structural, electronic properties and stability of the (1 × 1) $PbTiO_3$ (111) polar surfaces by first-principles calculations. *Appl. Surf. Sci.* **2009**, *255*, 8145–8152. [CrossRef]
105. Liu, W.; Wang, C.; Cui, J.; Man, Z.Y. Ab initio calculations of the $CaTiO_3$ (111) polar surfaces. *Solid State Commun.* **2009**, *149*, 1871–1876. [CrossRef]
106. Kim, J.S.; Kim, Y.C. Equilibrium crystal shape of $BaZrO_3$ and space charge formation in the (011) surface by using ab-initio thermodynamics. *J. Korean Phys. Soc.* **2017**, *70*, 75–80. [CrossRef]
107. Eglitis, R.I. Ab initio calculations of the atomic and electronic structure of $BaZrO_3$ (111) surfaces. *Solid State Ion.* **2013**, *230*, 43–47. [CrossRef]
108. Dovesi, R.; Saunders, V.R.; Roetti, C.; Orlando, R.; Zicovich-Wilson, C.M.; Pascale, F.; Civalleri, B.; Doll, K.; Harrison, N.M.; Bush, I.J.; et al. *CRYSTAL-2017 User Manual*; University of Torino: Turin, Italy, 2017.
109. Piskunov, S.; Heifets, E.; Eglitis, R.I.; Borstel, G. Bulk properties and electronic structure of $SrTiO_3$, $BaTiO_3$, $PbTiO_3$ perovskites: An ab initio HF/DFT study. *Comput. Mater. Sci.* **2004**, *29*, 165–178. [CrossRef]
110. Perdew, J.P.; Wang, Y. Accurate and simple density functional for the electronic exchange energy: Generalized gradient approximation. *Phys. Rev. B* **1986**, *33*, 8800–8802, Erratum in *Phys. Rev. B* **1989**, *40*, 3399. [CrossRef]
111. Perdew, J.P.; Wang, Y. Accurate and simple analytic representation of the electron-gas correlation energy. *Phys. Rev. B* **1992**, *45*, 13244–13249. [CrossRef]
112. Lee, C.; Yang, W.; Parr, R.G. Development of the Colle-Salvetti correlation-energy formula into a functional of the electron density. *Phys. Rev. B* **1988**, *37*, 785–789. [CrossRef]
113. Monkhorst, H.J. Special points for Brillouin-zone integrations. *Phys. Rev. B* **1976**, *13*, 5188. [CrossRef]
114. Piskunov, S.; Kotomin, E.A.; Heifets, E.; Maier, J.; Eglitis, R.I.; Borstel, G. Hybrid DFT calculations of the atomic and electronic structure for ABO_3 perovskite (001) surfaces. *Surf. Sci.* **2005**, *575*, 75–88. [CrossRef]
115. Nova, T.F.; Disa, A.S.; Fechner, M.; Cavalleri, A. Metastable ferroelectricity in optically strained $SrTiO_3$. *Science* **2019**, *364*, 1075–1079. [CrossRef]
116. Vanderbilt, D. First-principles theory of structural phase transitions in cubic perovskites. *J. Korean Phys. Soc.* **1998**, *32*, S103–S106.
117. Noguera, C. Polar oxide surfaces. *J. Phys. Condens. Matter* **2000**, *12*, R367. [CrossRef]
118. Tasker, P.W. The stability of ionic crystal surfaces. *J. Phys. C Solid State Phys.* **1979**, *12*, 4977. [CrossRef]
119. Pojani, A.; Finocchi, F.; Noguera, C. A theoretical study of the unreconstructed polar (111) face of $SrTiO_3$. *Appl. Surf. Sci.* **1999**, *142*, 177–181. [CrossRef]
120. Eglitis, R.I. Theoretical Modelling of the Energy Surface (001) and Topology of $CaZrO_3$ Perovskite. *Ferroelectrics* **2015**, *483*, 75–85. [CrossRef]
121. Hellwege, K.H.; Helwege, A.M. *Ferroelectrics and Related Substances*; Landolt-Bornstein, New Series, Group III; Springer: Berlin/Heidelberg, Germany, 1969; Volume 3.
122. Ali, R.; Yashima, M. Space group and crystal structure of the perovskite $CaTiO_3$ from 296 to 1720K. *J. Solid State Chem.* **2005**, *178*, 2867–2872. [CrossRef]
123. Mabud, S.A.; Glazer, A.M. Lattice parameters and birefringence in $PbTiO_3$ single crystals. *J. Appl. Crystallogr.* **1979**, *12*, 49–53. [CrossRef]
124. Mathews, M.D.; Mirza, E.B.; Momin, A.C. High-temperature X-ray diffractometric studies of $CaZrO_3$, $SrZrO_3$ and $BaZrO_3$. *J. Mater. Sci. Lett.* **1991**, *10*, 305–306. [CrossRef]
125. Aoyagi, S.; Kuroiwa, Y.; Sawada, A.; Tanaka, H.; Harada, J.; Nishibori, E.; Takata, M.; Sakata, M. Direct Observation of Covalency between O and Disordered Pb in Cubic $PbZrO_3$. *J. Phys. Soc. Jpn.* **2002**, *71*, 2353–2356. [CrossRef]
126. Kennedy, B.J.; Howard, C.J.; Chakoumakos, B.C. High-temperature phase transitions in $SrZrO_3$. *Phys. Rev. B* **1999**, *59*, 4023–4027. [CrossRef]
127. Mulliken, R.S. Electronic Population Analysis on LCAO-MO Molecular Wave Functions. *J. Chem. Phys.* **1955**, *23*, 1833–1840. [CrossRef]
128. Catlow, C.R.A.; Stoneham, A.M. Ionicity in solids. *J. Phys. C Solid State Phys.* **1983**, *16*, 4321. [CrossRef]
129. Bochiccio, R.C.; Reale, H.F. On the nature of crystalline bonding: Extension of statistical population analysis to two- and three-dimensional crystalline systems. *J. Phys. B At. Mol. Opt. Phys.* **1993**, *26*, 4871. [CrossRef]
130. Eglitis, R.I.; Kotomin, E.A.; Trepakov, V.A.; Kapphan, S.E.; Borstel, G. Quantum chemical modelling of electron polarons and "green" luminescence in $PbTiO_3$ perovskite crystals. *J. Phys. Condens. Matter* **2002**, *14*, L647. [CrossRef]
131. Wemple, S.H. Polarization Fluctuations and the Optical-Absorption Edge in $BaTiO_3$. *Phys. Rev. B* **1970**, *2*, 2679–2689. [CrossRef]

132. Benthem, K.; Elsässer, C.; French, R.H. Bulk electronic structure of $SrTiO_3$: Experiment and theory. *J. Appl. Phys.* **2001**, *90*, 6156–6164. [CrossRef]
133. Robertson, J. Band offsets of wide-band-gap oxides and implications for future electronic devices. *J. Vac. Sci. Technol. B* **2000**, *18*, 1785–1791. [CrossRef]
134. Meyer, B.; Padilla, J.; Vanderbilt, D. Theory of $PbTiO_3$, $BaTiO_3$, and $SrTiO_3$ surfaces. *Faraday Discuss.* **1999**, *114*, 395–405. [CrossRef]
135. Wang, Y.X.; Arai, M.; Sasaki, T.; Wang, C.L. First-principles study of the (001) surface of cubic $CaTiO_3$. *Phys. Rev. B* **2006**, *73*, 035411. [CrossRef]
136. Bickel, N.; Schmidt, G.; Heinz, K.; Müller, K. Ferroelectric relaxation of the $SrTiO_3$ (100) surface. *Phys. Rev. Lett.* **1989**, *62*, 2009–2011. [CrossRef] [PubMed]
137. Hikita, T.; Hanada, M.; Kudo, M.; Kawai, M. Structure and electronic state of the TiO_2 and SrO terminated $SrTiO_3$ (100) surfaces. *Surf. Sci.* **1993**, *287–288*, 377–381. [CrossRef]
138. Wang, Y.X.; Arai, M. First-principles study of the (001) surface of cubic $SrZrO_3$. *Surf. Sci.* **2007**, *601*, 4092–4096. [CrossRef]

Disclaimer/Publisher's Note: The statements, opinions and data contained in all publications are solely those of the individual author(s) and contributor(s) and not of MDPI and/or the editor(s). MDPI and/or the editor(s) disclaim responsibility for any injury to people or property resulting from any ideas, methods, instructions or products referred to in the content.